

Absolute dimensions of eclipsing binaries. XXIX. *

The Am-type systems SW Canis Majoris and HW Canis Majoris. **

G. Torres¹, J. V. Clausen^{2***}, H. Bruntt^{2,3}, A. Claret⁴, J. Andersen², B. Nordström², R. P. Stefanik¹, and D. W. Latham¹

¹ Harvard-Smithsonian Center for Astrophysics, 60 Garden Street, Cambridge, MA 02138, USA

² Niels Bohr Institute, Copenhagen University, Juliane Maries Vej 30, DK-2100 Copenhagen Ø, Denmark

³ School of Physics A28, University of Sydney, 2006 NSW, Australia

⁴ Instituto de Astrofísica de Andalucía, Apartado 3004, 18080 Granada, Spain

Received 02 Aug 2011 / Accepted xx Dec 2011

ABSTRACT

Context. Accurate physical properties of eclipsing stars provide important constraints on models of stellar structure and evolution, especially when combined with spectroscopic information on their chemical composition. Empirical calibrations of the data also lead to accurate mass and radius estimates for exoplanet host stars. Finally, accurate data for unusual stellar subtypes, such as Am stars, also help to unravel the cause(s) of their peculiarities.

Aims. We aim to determine the masses, radii, effective temperatures, detailed chemical composition and rotational speeds for the Am-type eclipsing binaries SW CMa (A4-5m) and HW CMa (A6m) and compare them with similar normal stars.

Methods. Accurate radial velocities from the Digital Speedometers of the Harvard-Smithsonian Center for Astrophysics were combined with previously published *wby* photometry to determine precise physical parameters for the four stars. A detailed abundance analysis was performed from high-resolution spectra obtained with the Nordic Optical Telescope (La Palma).

Results. We find the masses of the (relatively evolved) stars in SW CMa to be 2.10 and 2.24 M_{\odot} , with radii of 2.50 and 3.01 R_{\odot} , while the (essentially zero-age) stars in HW CMa have masses of 1.72 and 1.78 M_{\odot} , radii of 1.64 and 1.66 R_{\odot} – all with errors well below 2%. Detailed atmospheric abundances for one or both components were determined for 14 elements in SW CMa ([Fe/H] = +0.49/+0.61 dex) and 16 in HW CMa ([Fe/H] = +0.33/+0.32 dex); both abundance patterns are characteristic of metallic-line stars. Both systems are well fit by current stellar evolution models for assumed bulk abundances of [Fe/H] = +0.05 and +0.23, respectively ([α /Fe] = 0.0), and ages of \sim 700 Myr and 160 Myr.

Key words. Stars: binaries: eclipsing – Stars: fundamental parameters – Stars: abundances – Stars: chemically peculiar – Stars: individual: SW CMa – Stars: individual: HW CMa

1. Introduction

Among the eclipsing binaries with the best determined fundamental properties approximately two dozen are of spectral type A (see Torres et al. 2010). Roughly 20–30%

Send offprint requests to: G. Torres,

e-mail: gtorres@cfa.harvard.edu

* Based on observations carried out with the Nordic Optical Telescope (NOT) at La Palma, the 50 cm Strömgren Automatic Telescope (SAT) at ESO, La Silla, the 1.5 m Wyeth reflector at the Oak Ridge Observatory, Harvard, Massachusetts, USA, and the 1.5 m Tillinghast reflector at the F. L. Whipple Observatory, Mt. Hopkins, Arizona, USA.

** Tables A.1 and A.2 as well as Appendices B and C will be available in electronic form at the CDS via anonymous ftp to 130.79.128.5 or via <http://cdsweb.u-strasbg.fr/Abstract.html>.

*** Deceased.

of main-sequence A stars are known to be metallic-lined (Am). The Am stars are found overwhelmingly to be in binary systems (e.g., Abt 1961). They are characterized by peculiar abundance patterns including a deficiency of light elements such as Sc and Ca, enhancement of iron-peak elements, and a strong overabundance of Sr and some rare earths, sometimes by an order of magnitude or more. The enhancement generally increases with increasing atomic number. Their typically slower axial rotation and stronger metal lines compared to normal A stars tend to facilitate the radial-velocity measurements necessary for accurate mass determinations. It is therefore not surprising that systems with Am stars are over-represented among the best-measured eclipsing binaries: fully half of the A-type systems for which we know the absolute masses and radii

with relative errors less than 3% contain at least one component showing these abundance abnormalities.

Although significant progress in understanding and modeling these chemically peculiar objects has been made in recent years, important questions regarding the role of rotation and the origin of the detailed patterns of element enhancement and depletion are not yet completely settled (see, e.g., Abt 2000, Böhm-Vitense 2006, Vick et al. 2010). Further observational constraints are highly desirable, particularly ones in which very accurate mass and radius determinations are accompanied by a detailed abundance study of the components.

Beyond a qualitative assessment of their metallic-lined nature, individual element abundances are known for precious few of the dozen or so Am binaries with well determined properties (see, e.g., Lyubimkov et al. 1996). Thus, little can be said about whether or how the detailed abundance patterns that seem to vary to some degree from star to star depend on global properties such as mass, effective temperature, or surface gravity. In this paper we present extensive new observations of two eclipsing Am systems, SW CMa and HW CMa, with the goal of determining not only accurate absolute dimensions but also individual abundances for all four stars. It is hoped that these results and others like them will present an opportunity for advancement on some of the issues mentioned above. Figure 1 places the two systems in the context of all other main sequence eclipsing binaries in the same mass regime that have the best-determined masses and radii. Am stars are marked with open circles. SW CMa is seen to be among the more evolved cases, while HW CMa is the least evolved in this mass range.

We describe below our spectroscopic observations of these systems, and an analysis of those data along with previously-published high-precision four-color Strömgren photometry in order to obtain accurate masses and radii. For SW CMa our determinations substantially improve upon previous estimates; for HW CMa they represent the first such measurements. We conclude with a detailed comparison with models of stellar and tidal evolution.

2. SW CMa

The observational history of SW CMa (HD 54520, HIP 34431, $V = 9.15$, A4–A5) has been summarized by Clausen et al. (2008). Since its discovery as an eclipsing binary by Hoffmeister (1932), relatively little progress in understanding its physical properties was made in more than six decades until the most recent study by Lacy (1997). In that work photoelectric UBV light curves were combined with new spectroscopy to yield the first precise determination of the masses and radii for the components. The orbit is eccentric, and apsidal motion was detected by Lacy (1997) and subsequently refined by Clausen et al. (2008), although the apsidal period is very long and still poorly constrained ($U = 14\,900 \pm 4\,700$ yr).

For the analysis in this paper we adopt the linear ephemeris derived by Clausen et al. (2008),

$$\text{Min I (HJD)} = 2\,446\,829.6482(1) + 10^d 091988(5) \times E,$$

in which the uncertainties in the period and reference epoch are indicated in parentheses in units of the last decimal place. This corresponds to the eclipse of the more massive and slightly hotter component. The secondary eclipse occurs approximately at phase 0.31.

2.1. Radial velocities and spectroscopic orbit

The spectroscopic observations of SW CMa used here for the radial-velocity determinations were carried out at the Harvard-Smithsonian Center for Astrophysics (CfA) between 1988 April and 1989 March. A total of 39 spectra were gathered with the 1.5 m Wyeth reflector at the Oak Ridge Observatory (Harvard, Massachusetts). Two additional spectra were taken using the 1.5 m Tillinghast reflector at the F. L. Whipple Observatory on Mt. Hopkins, Arizona. Nearly identical spectrographs (“Digital Speedometers” (DS); Latham 1992) were used on each telescope, equipped with photon-counting Reticon detectors that recorded a single echelle order 45 Å wide centered at a wavelength near 5187 Å (Mg I b triplet). The resolving power of these instruments is $\lambda/\Delta\lambda \approx 35\,000$, and the signal-to-noise (S/N) ratios of the 41 spectra we collected range from 10 to 25 per resolution element of 8.5 km s^{-1} .

Radial velocities were obtained with TODCOR, a two-dimensional cross-correlation technique introduced by Zucker & Mazeh (1994). Templates for the cross-correlations were selected from a library of synthetic spectra based on model atmospheres by R. L. Kurucz, which has been described by Nordström et al. (1994) and Latham et al. (2002). The parameters of these templates are the effective temperature (T_{eff}), metallicity ($[m/H]$), rotational velocity ($v \sin i$, when seen in projection), and surface gravity ($\log g$).

The optimal templates for the two components were determined by running extensive grids of cross-correlations and selecting the combination of parameters yielding the highest correlation averaged over all exposures, weighted by the strength of each spectrum (see Torres et al. 2002). The surface gravities were held fixed at $\log g = 4.0$ for both stars, close to the final values in Sect. 2.4. Temperatures and rotational velocities were optimized for a range of different (fixed) metallicities, and the first hint that the stars have anomalously strong metal lines came from the fact that the highest cross-correlation value was obtained for the largest metallicity available in our grid, $[m/H] = +0.5$, for both components. It is possible that a better match to the observed spectra could be found for an even higher metallicity, and from the trend of the improvement with $[m/H]$, the effect appears somewhat more pronounced for the secondary.

By interpolation the optimal temperatures were found to be 8210 K and 7860 K, and the best $v \sin i$ values are

29 km s⁻¹ and 15 km s⁻¹. However, other photometric and spectroscopic estimates discussed later point toward very similar T_{eff} values for the two stars, as opposed to the 350 K difference implied above. Our primary star T_{eff} estimate is in agreement with those determinations, but the secondary value seems too cool. Due to the limited wavelength coverage of the CfA spectra, metallicity is strongly correlated with effective temperature so that an almost equally good fit to the spectra can be found for different template combinations in which the stronger lines corresponding to a metal-rich composition can be made to appear weaker by increasing the temperature, and vice versa. Therefore, even though we cannot go any higher in [m/H] in our optimization scheme, a satisfactory match to the observed spectra can still be found by adjusting the temperature. This is likely the explanation for the excessively cool T_{eff} we derive for the secondary from these spectra, which supports the notion that this star may have a more anomalous (generally more metal-rich) composition than the primary. Experience shows that this degeneracy has little impact on the radial velocities themselves, although it does of course limit our ability to simultaneously infer accurate values of [m/H] and T_{eff} . For the velocity determinations we adopted [m/H] = +0.5 for both stars, along with temperatures of 8250 K and 7750 K and $v \sin i$ parameters of 30 km s⁻¹ and 16 km s⁻¹ for the primary and secondary. These are the values in our grid nearest to the optimal estimates mentioned earlier. We do not attach any astrophysical meaning to these T_{eff} values, but treat them merely as adjustable parameters intended to provide the best radial velocities, as free as possible from biases.

The stability of the velocity zero point during the period of observation was monitored by taking exposures of the dusk and dawn sky. Small run-to-run corrections were applied in the manner described by Latham (1992). Additional systematic errors may occur because of the narrow wavelength coverage of the CfA spectra and the fact that lines move in and out of the spectral window as a function of orbital phase and the heliocentric correction (see Latham et al. 1996). To investigate this we performed experiments with simulated double-lined spectra following the procedure detailed by Torres et al. (1997), and corrections based on them were then applied to the raw velocities. For SW CMA these corrections are typically small (< 1 km s⁻¹), and their net effect is to increase the absolute masses by slightly less than 0.4%, and the radii by about 0.1%. They are shown in Fig. 2, where the systematic pattern is obvious, particularly in the lower panel.

The final radial velocities referred to the heliocentric frame are presented in Table A.1 of Appendix A (available electronically), and include all corrections mentioned above. The elements of the orbital solution we obtain from them are listed in Table 1, along with derived quantities including the minimum masses and semimajor axes. The measurements and the fitted orbit are shown in Fig. 3 together with the residuals. The larger rms residual for the primary, despite being the brighter star, is explained by the significantly higher rotational broadening compared to

Table 1. Spectroscopic orbital solution for SW CMA.

Parameter	Value
Adjusted quantities:	
K_p (km s ⁻¹)	82.09 ± 0.35
K_s (km s ⁻¹)	87.37 ± 0.22
γ (km s ⁻¹)	+42.57 ± 0.17
e	0.3174 ± 0.0011
ω (°) ^a	163.26 ± 0.51
Adopted quantities:	
P (days)	10.091988
T_1 (HJD-2 400 000) ^b	46829.6482
Derived quantities:	
$M_p \sin^3 i$ (M_\odot)	2.237 ± 0.014
$M_s \sin^3 i$ (M_\odot)	2.102 ± 0.018
$q \equiv M_s/M_p$	0.9396 ± 0.0048
$a_p \sin i$ (10 ⁶ km)	10.803 ± 0.046
$a_s \sin i$ (10 ⁶ km)	11.498 ± 0.029
$a \sin i$ (R_\odot)	32.057 ± 0.076
Other quantities pertaining to the fit:	
N_{obs}	41
Time span (days)	333
σ_p (km s ⁻¹)	1.93
σ_s (km s ⁻¹)	1.19

^a Longitude of periastron for the more massive star.

^b Time of central primary eclipse (eclipse of the more massive star).

the secondary. We note that while our secondary velocity semi-amplitude agrees with the value reported by Lacy (1997), our primary semi-amplitude is slightly larger (by 2%, a 1.6- σ difference).

In addition to the radial velocities, we used TODCOR to derive the light ratio at the mean wavelength of our observations (5187 Å), following Zucker & Mazeh (1994). We obtain $L_s/L_p = 0.68 \pm 0.04$ (secondary/primary).

2.2. Chemical abundances

In order to obtain reliable estimates of the spectroscopic properties, a spectrum of SW CMA was obtained on UT 2008 November 17 (mid exposure at HJD 2 454 787.65730, orbital phase 0.5472) using the FIES instrument (Frandsen & Lindberg 1999) on the 2.5 m Nordic Optical Telescope (NOT) on La Palma, with a resolving power of $\lambda/\Delta\lambda \approx 46\,000$. The signal-to-noise ratio achieved is about 60 per pixel in the 6160 Å region, and the wavelength coverage is approximately 3600–7400 Å recorded in 78 echelle orders. Reductions used the IRAF-based FIEStool package¹ with nightly flatfield, bias, and dark frames, as well as thorium-argon exposures taken immediately before and after the science exposure.

¹ See <http://www.not.iac.es> for details on FIES and FIEStool.

The spectroscopic analysis was carried out with the IDL-based VWA analysis tool, extended to the analysis of double-lined spectra (for details of the procedure, we refer the reader to Bruntt et al. 2004, 2008, 2009). Briefly, VWA uses the SYNTH software (Valenti & Piskunov 1996) to generate synthetic spectra. Atmosphere models are interpolated from the recent grid of MARCS model atmospheres (Gustafsson et al. 2008), which adopt the solar composition by Grevesse et al. (2007). Line information was taken from the Vienna Atomic Line Database (VALD; Kupka et al. 1999). In deriving abundances relative to the Sun, the $\log gf$ values were adjusted in such a way that each measured line in the Wallace et al. (1998) solar atlas reproduces the atmospheric abundances by Grevesse et al. (2007).

The number of unblended lines for the analysis is somewhat limited in this case due to the relatively large rotational broadening. We restricted the measurements to lines with equivalent widths smaller than about 65 mÅ in the composite spectrum (corresponding to about 110 mÅ for the primary and 160 mÅ for the secondary), and the surface gravities were held fixed to preliminary values near those given in later Table 4. We assumed a light ratio of $L_s/L_p = 0.69$ (V band), from the light-curve solutions described below. The effective temperatures and micro-turbulent velocities ($v_{\text{mic}} = 2.70 \text{ km s}^{-1}$ and 2.85 km s^{-1} for the primary and secondary, with estimated errors of 0.8 km s^{-1}) were adjusted to yield consistent values for the abundances of Fe I and Fe II, and to avoid correlations with the equivalent width and excitation potential. The results for T_{eff} indicate similar values for the primary and secondary of $8200 \pm 150 \text{ K}$ and $8100 \pm 150 \text{ K}$, respectively, corresponding approximately to spectral types A4 or A5.

Individual abundances on the scale of the Grevesse et al. (2007) solar abundances were determined separately in one or both stars for 14 species. These results are listed in Table 2, along with the number of spectral lines used in each case. Abundances based on fewer than three lines are somewhat more uncertain. NLTE effects become significant in stars with temperatures hotter than about 8000 K, so appropriate corrections to the abundances of Fe I (+0.13 dex and +0.11 dex for the primary and secondary) have been included in the values we report, following Rentzsch-Holm (1996). The average iron abundances for the components are $[\text{Fe}/\text{H}] = +0.49 \pm 0.15$ and $+0.61 \pm 0.15$, where the uncertainties include a contribution from the errors in temperature and v_{mic} . Figure 4 displays the abundance pattern for both stars in SW CMa. Although some of these determinations are rather uncertain due to the small number of lines and limited signal-to-noise ratio of our spectroscopic material, the enhanced iron-peak abundances compared to calcium, and especially the strong overabundance of heavy elements such as Sr, Y, and Ba, are typical of Am stars and suggest that both components are chemically peculiar. The iron abundance, as well as the Fe/Ca difference (0.44 and 0.81 dex), is somewhat larger for the secondary than the primary, consistent with the hints we saw in the CfA spectra. The pro-

Table 2. Abundances for the components of SW CMa.

Element	Primary			Secondary		
	[X/H]	σ	N	[X/H]	σ	N
Na I	+0.57		1			
Mg I	+0.21		1			
Si I				-0.51		2
Si II	+0.20		2			
Ca I	+0.05	0.17	3	-0.20	0.16	4
Ti II	+0.02	0.21	3	+0.37	0.12	3
Cr II	+0.15		2	+0.19		1
Fe I	+0.50	0.09	17	+0.59	0.10	22
Fe II	+0.47	0.09	11	+0.63	0.11	15
Ni I	+0.51		2	+0.42		2
Zn I	+1.08		2	+1.06		1
Sr II	+1.00		1	+1.29		1
Y II	+1.02		1	+1.11		1
Ba II	+1.40	0.21	3	+1.54		2

NOTE: These abundances are based on $v_{\text{mic}} = 2.70 \text{ km s}^{-1}$ and 2.85 km s^{-1} for the primary and secondary, respectively, and $[\text{Fe}/\text{H}] = +0.45$ for the model atmospheres applied in the analysis. Fe I abundances include corrections for NLTE. N represents the number of lines of each element, and σ is the scatter of the measurements (listed only if $N > 2$).

jected rotational velocities were measured from the FIES spectrum by synthesizing line profiles for a dozen isolated lines and comparing them with the observed spectrum, seeking to minimize the residual differences. The adopted macroturbulence velocity was $\zeta_{\text{RT}} = 8 \text{ km s}^{-1}$ for both components, extrapolated from the trend with temperature reported by Gray (2005). We obtained $v \sin i$ values of $24.0 \pm 1.5 \text{ km s}^{-1}$ and $10.0 \pm 1.0 \text{ km s}^{-1}$ for the primary and secondary, respectively. That these rotational velocities are much slower than typical for A stars in the field is a general characteristic found in other Am stars as well (see, e.g., Abt & Morrell 1995, Abt 2000, Fossati et al. 2008).²

2.3. Photometric elements

For this analysis we make use of the differential photometry for SW CMa in the Strömgren system that has been reported previously by Clausen et al. (2008). As described there, the *uvby* light curves consist of 820 observations in each band collected with the 0.5 m Strömgren Automatic Telescope at ESO (La Silla), on 89 nights during five periods between 1987 February and 1991 March. The average uncertainty per differential observation is about 5 mmag in *vby* and 6 mmag in *u*, and the measurements scatter at these same levels throughout all phases, indicating that the components of SW CMa are constant within the pre-

² Note, however, that slow rotation in an A star is not always associated with chemical peculiarity (see, e.g., Fekel et al. 2006).

Table 3. Adopted photometric elements for SW CMa.

i ($^\circ$)	88.59 ± 0.20			
$e \cos \omega$	-0.30313 ± 0.00009			
$e \sin \omega$	$+0.0883 \pm 0.0017$			
e	0.3157 ± 0.0004			
ω ($^\circ$)	163.76 ± 0.29			
$r_p + r_s$	0.1718 ± 0.0010			
k	0.827 ± 0.018			
r_p	0.0940 ± 0.0006			
r_s	0.0778 ± 0.0013			
	y	b	v	u
J_s	1.013	1.012	0.996	1.020
	± 3	± 2	± 3	± 4
L_s/L_p	0.693	0.692	0.681	0.697
	± 30	± 18	± 15	± 33

NOTE: The individual flux and luminosity ratios are based on the mean stellar and orbital parameters.

cision of the data. Compared to the UBV light curves in the earlier study by Lacy (1997), the present observations are roughly twice as numerous and provide better orbital coverage, particularly at the shoulders of the minima.

Light-curve solutions were performed with the JKTEBOP code (Southworth et al. 2004a, 2004b), which is an updated and expanded version of the original EBOP program based on the Nelson-Davis-Etzel model (Nelson & Davis 1972; Etzel 1981). This model represents the binary components as biaxial ellipsoids and applies a simple bolometric reflection prescription, but is perfectly adequate for the stars in SW CMa given their very small deformation (oblateness of 0.0012 for the primary and 0.0008 for the secondary, both much smaller than the tolerance for this model of 0.04; see Popper & Etzel 1981). Each of the $uvby$ light curves was analyzed independently adopting the ephemeris given in Sect. 2, with equal weight assigned to all observations. The main parameters solved for are the radius ratio between the secondary and the primary ($k \equiv r_s/r_p$), the sum of the radii ($r_p + r_s$), the inclination angle (i), the geometric factors $e \sin \omega$ and $e \cos \omega$, the central surface brightness ratio of the secondary in terms of the primary (J_s), a photometric scale factor (the magnitude at quadrature), and a correction to the phase of the primary minimum. The mass ratio was held fixed at the value determined spectroscopically (Sect. 2.1). Gravity darkening coefficients, y_p and y_s , were computed from a simple Planck approximation (see, e.g., Martynov 1973). Initial solutions were carried out with limb-darkening (LD) coefficients interpolated from theoretical calculations (van Hamme 1993, and ATLAS version of the Claret 2000 tables) according to the effective temperatures and surface gravities for stars as determined here.³

³ Solar metallicity was adopted in interpolating all limb-darkening coefficients for consistency in the comparison be-

We found good agreement between the results from the $uvby$ passbands, although small systematic differences were noticed between fits using LD coefficients from different sources, as described in detail in Appendix B (available electronically). In view of this, and out of concern that imposing LD coefficients from theory might introduce subtle biases in the geometric elements, for the final fits we chose to leave the LD coefficients free (linear law), with the only constraint that they be equal for the primary and secondary given that the temperatures are also very nearly the same. Additional experiments with LD free were carried out to explore the effect of including third light (ℓ_3) as an extra parameter. For all four passbands we found that ℓ_3 was negligible compared to its error, and we conclude third light is not significant.

The results are presented in Table 3, in which the values from the separate passbands have been averaged together, with weights inversely proportional to the rms residual of each solution. The uncertainties listed in the table were obtained by running 1000 Monte Carlo simulations with JKTEBOP, and we consider them to be more realistic than the formal (internal) errors from the solutions presented in Appendix B. For the relative radii we also computed uncertainties by propagating the errors in $r_p + r_s$ and k following Torres et al. (2000). This procedure assumes the sum and ratio of the radii are uncorrelated, and results in uncertainties that are more nearly equal (0.0011 and 0.0010 for r_p and r_s , respectively) than those from Monte Carlo. However, the Monte Carlo simulations indicate that in this case $r_p + r_s$ and k are in fact correlated, invalidating the error propagation approach for SW CMa. The radiative quantities in Table 3 were computed from additional solutions in which the geometry was held fixed to the weighted average from the four bands. The eccentricity and longitude of periastron are more precise than, but consistent with those obtained spectroscopically, differing by 1.5σ and 0.9σ , respectively. The light ratios in b and y ($L_s/L_p = 0.69 \pm 0.02$ and 0.69 ± 0.03) are in excellent agreement with the value from our spectroscopic observations in Sect. 2.1 (0.68 ± 0.04 at 5187 Å). According to the final light-curve elements, 72% of the light of the primary is blocked at the deeper minimum. The secondary eclipse is nearly total: 97% of the y -band light of that star lost at that phase.

The light curves along with our best fit models appear in Fig. 5, and expanded views of the primary and secondary minima are shown in Fig. 6 and Fig. 7. The $O - C$ residuals are displayed in the bottom panels.

tween the different LD tables, given that the van Hamme (1993) calculations do not reach metallicities as high as those measured for SW CMa. However, inspection of the Claret (2000) calculations shows that the coefficients for $[\text{Fe}/\text{H}] = 0.0$ and $[\text{Fe}/\text{H}] = +0.5$ differ very little.

Table 4. Astrophysical properties of the SW CMA system.

	Primary	Secondary
Absolute dimensions:		
$M (M_{\odot})$	2.239 ± 0.014	2.104 ± 0.018
$R (R_{\odot})$	3.014 ± 0.020	2.495 ± 0.042
$\log g$ (cgs)	3.8298 ± 0.0065	3.967 ± 0.015
$v \sin i$ (km s ⁻¹) ^a	24.0 ± 1.5	10.0 ± 1.0
v_{sync} (km s ⁻¹) ^b	15.1 ± 0.1	12.5 ± 0.2
v_{psync} (km s ⁻¹) ^c	24.5 ± 0.2	20.3 ± 0.3
v_{peri} (km s ⁻¹) ^d	30.6 ± 0.2	25.3 ± 0.4
Radiative and other properties:		
T_{eff} (K)	8200 ± 150	8100 ± 150
M_{bol} (mag)	0.817 ± 0.081	1.281 ± 0.088
$\log L/L_{\odot}$	1.566 ± 0.032	1.380 ± 0.035
BC_V (mag)	$+0.02 \pm 0.10$	$+0.02 \pm 0.10$
M_V (mag)	0.79 ± 0.12	1.26 ± 0.13
Distance (pc)	576 ± 27	
$V - M_V$ (mag)	8.80 ± 0.10	
[Fe/H] ^e	$+0.49 \pm 0.15$	$+0.61 \pm 0.15$
Photometric indices:		
V ^f	9.721 ± 0.021	10.119 ± 0.029
$(b - y)$ ^f	0.093 ± 0.012	0.095 ± 0.014
m_1 ^f	0.203 ± 0.012	0.220 ± 0.013
c_1 ^f	1.031 ± 0.015	0.987 ± 0.020
$E(b - y)$	0.023 ± 0.010	

^a Measured projected rotational velocity.

^b $v \sin i$ expected for synchronous rotation.

^c $v \sin i$ expected for pseudo-synchronous rotation.

^d Expected $v \sin i$ if synchronized at periastron.

^e Values representative of the surface layers only.

^f Not corrected for interstellar absorption/reddening.

NOTE: The bolometric corrections (BC_V) are adopted from Flower (1996), along with with $T_{\text{eff}\odot} = 5780$ K, and $M_{\text{bol}\odot} = 4.73$ (see Torres 2010). An additional error contribution of 0.10 mag is added in quadrature to the BC_V uncertainty propagated from the temperature uncertainties.

2.4. Absolute dimensions

Our spectroscopy and differential photometry for SW CMA yield masses with uncertainties of 0.6% and 0.9% for the primary and secondary, and radii that are good to 0.7% and 1.7%, respectively. The values of M and R are consistent with the analysis by Lacy (1997), but our errors are generally smaller (by about a factor of three in the case of the masses).⁴ We list the masses and radii in Table 4, along with other derived properties.

Interstellar reddening may be estimated from the $uvby\beta$ indices out of eclipse reported by Clausen et al. (2008), which agree well with those of Wolf & Kern (1983). Using the calibration by Crawford (1979) we obtain $E(b - y) = 0.023$, to which we assign a conservative uncertainty of 0.01 mag. We adopt this value in the fol-

lowing. The corresponding visual extinction is $A(V) = 0.10 \pm 0.04$. Other estimates of the extinction in the direction of SW CMA may be inferred from dust maps (which measure the *total* extinction), after proper correction for the distance to the system by iterations. However, we find those estimates to be larger and rather discrepant: from Hakkila et al. (1997) we obtain $A(V) = 0.16$, corresponding to $E(b - y) = 0.037$, while the maps of Schlegel et al. (1998) suggest $A(V) = 0.32$, or $E(b - y) = 0.077$, at the distance to the system.

The combined $uvby$ indices from Clausen et al. (2008) and the light ratios from our photometric solutions yield the individual indices for the components, also listed in Table 4. The uncertainties include the contribution from all observational errors. The individual bolometric luminosities follow from the spectroscopic temperatures and the radii, and the distance was obtained from the luminosities, the de-reddened V magnitude, and bolometric corrections from Flower (1996). We infer a distance to the system of 576 ± 27 pc, and separate calculations for the primary and secondary agree closely (giving 583 ± 36 pc and 566 ± 37 pc, respectively), which is an indication of good internal consistency. Knowledge of the individual photometric indices for the components provides an opportunity to derive temperature estimates as a check on the spectroscopic values, to the extent that existing temperature calibrations for normal A-type stars can be applied to objects displaying the Am phenomenon. This appears to be the case, according to Netopil et al. (2008). After correcting the individual indices for the effects of interstellar reddening, application of the calibration of Napiwotzki et al. (1993) leads to estimates of 8188 ± 157 K and 8168 ± 173 K for the primary and secondary, in good accord with the spectroscopic values. A 0.02 mag error in $b - y$ changes these results by about 200 K. Using the central surface brightness ratio J_s in the y band obtained from our light curve solutions with the flux calibration by Popper (1980) yields an estimate of the temperature difference between the stars of $\Delta T_{\text{eff}} = -32$ K, suggesting the secondary (less massive star) is marginally hotter than the primary, though well within the uncertainties of our other determinations.

The $v \sin i$ values discussed in Sect. 2.1 that provide the best fit to the CfA spectra are 29 ± 3 km s⁻¹ and 15 ± 2 km s⁻¹ for the primary and secondary, respectively. Strictly speaking, however, these measures represent the *total* line broadening, and not just rotation, and indeed they are systematically larger than those obtained from the FIES spectrum (24.0 ± 1.5 km s⁻¹ and 10.0 ± 1.0 km s⁻¹). This is most likely due to the fact that the synthetic templates used to analyze the CfA spectra have been calculated with a radial-tangential macroturbulent velocity appropriate for solar-type stars ($\zeta_{\text{RT}} = 1.5$ km s⁻¹), whereas the values of ζ_{RT} expected for A-type stars (at least normal ones) are significantly higher (see, e.g., Gray 2005). Indeed, for the FIES analysis we adopted $\zeta_{\text{RT}} = 8$ km s⁻¹. We therefore rely on the FIES determination of $v \sin i$, which we report in Table 4. Also

⁴ We note that the uncertainty of $0.5 M_{\odot}$ for the primary mass reported in Lacy's Table 7 is likely a misprint; we have assumed it should read $0.05 M_{\odot}$.

listed there are the $v \sin i$ values predicted if the stars had their spins synchronized with the mean orbital motion (v_{sync}), with the motion at periastron (v_{peri}), and with an intermediate equilibrium rate of ‘pseudo-synchronization’ (see Hut 1981). The comparison would suggest the primary component of SW CMa is rotating at the pseudo-synchronous rate and the secondary is spinning considerably more slowly than pseudo-synchronous. We note here also that Lacy (1997) measured rather different values for $v \sin i$ of $30 \pm 2 \text{ km s}^{-1}$ for the primary and $21 \pm 3 \text{ km s}^{-1}$ for the secondary, which would lead to different conclusions regarding synchronization.

The Am nature of both stars is supported by the abundance pattern we see, most notably that the heavy elements are overabundant by an order of magnitude or more compared to solar. Enhancements seem rather similar for the two components, with a few exceptions noted earlier.

3. HW CMa

The long-period eclipsing binary HW CMa (HD 54549, $V = 9.19$, A6, $P = 21.1$ days) was discovered serendipitously by Liu et al. (1992) in the course of spectroscopic monitoring of SW CMa, which is only about 2.5 away. Beyond the initial estimates of the minimum masses by these authors ($1.74 M_{\odot}$ and $1.80 M_{\odot}$), no determinations of the absolute dimensions have been reported in the literature. Accurate differential *uvby* photometry of HW CMa was published by Clausen et al. (2008), who confirmed that the combination of high orbital eccentricity ($e \approx 0.50$), low inclination ($i \approx 84.7^{\circ}$), and a line of apsides practically aligned with the line of sight result in the complete absence of eclipses near apastron. The shallow (0.13 mag) eclipses that do take place near periastron correspond to the less massive star being occulted by the other. In the following we refer to these as the primary eclipses, following the convention adopted by Clausen et al. (2008). Secondary eclipses would be expected at phase ~ 0.52 , but as mentioned above, they do not occur.

An accurate ephemeris has been determined by Clausen et al. (2008) as

$$\text{Min I (HJD)} = 2\,452\,279.6787(4) + 21^{\text{d}}1178329(33) \times E,$$

which we adopt here. Apsidal motion is expected in view of the large eccentricity, but due to the lack of secondary eclipses this can only be measured spectroscopically.

3.1. Radial velocities and spectroscopic orbit

Spectroscopic observations of HW CMa were gathered between 1988 November and 1999 March with the same instrumentation used for SW CMa and described in Sect. 2.1. A total of 48 spectra were included in the analysis, with S/N ratios ranging from 9 to 39 per resolution element of 8.5 km s^{-1} . This is a superset of the observations reported by Liu et al. (1992), who used the same spectrographs. The optimization of the synthetic templates

and determination of radial velocities using TODCOR follows the procedures described earlier. The surface gravities for the templates were held fixed at $\log g = 4.0$ for both stars, which is the value in our grid of synthetic spectra closest to the final estimates reported in Sect. 3.4. As was the case for SW CMa, cross-correlation grids with TODCOR indicated a preference for a metallicity of $[\text{Fe}/\text{H}] = +0.50$ for both stars, the highest available in our library of templates, but in this case we saw no obvious difference between the two stars. A value this high is again a hint of the possible Am nature of the components. The template parameters adopted for the RV determinations are $T_{\text{eff}} = 7500 \text{ K}$ (less massive star, the ‘primary’) and $T_{\text{eff}} = 7750 \text{ K}$ (more massive ‘secondary’), and $v \sin i = 16 \text{ km s}^{-1}$ for both components.

Simulations with synthetic binary spectra were run in the same way as for SW CMa to estimate and correct for systematic errors in the raw velocities resulting from lines shifting in and out of our narrow spectral window with orbital phase. The magnitude of these effects for HW CMa is less than 1 km s^{-1} (see Fig. 8). Nevertheless, the impact on the masses and radii is not negligible in this case: the masses increase by about 1% (~ 1.5 times their final errors), and the radii by slightly more than 0.3%. The final velocities including these corrections are listed in Table A.2, and incorporate also the adjustments for instrumental shifts from run to run described in Sect. 2.1. The RV measurements and our best-fit spectroscopic orbital solution are shown graphically in Fig. 9, and the elements are given in Table 5. The light ratio inferred from the CfA spectra using TODCOR is $L_p/L_s = 0.92 \pm 0.04$ (primary/secondary), which corresponds to the mean wavelength of those observations.

The final surface gravities of the stars ($\log g \approx 4.24$; Sect. 3.4) are approximately halfway between two steps in our library of templates, and our velocity determinations above used the lower of the two values ($\log g = 4.0$). Given that effective temperatures are strongly correlated with surface gravity in determinations based on our CfA spectra, a more accurate temperature may be derived by interpolation to $\log g = 4.24$. In this way we find $T_{\text{eff}} = 7630 \pm 150 \text{ K}$ and $7780 \pm 150 \text{ K}$ for the primary and secondary, and $v \sin i$ values (including other sources of line broadening; see Sect. 3.4) of 15 km s^{-1} for both stars. We expect the temperatures to be more accurate than in the case of SW CMa, as the line strengths of the two stars in HW CMa appear more or less equally enhanced compared to solar metallicity stars.

3.2. Chemical abundances

For a detailed study of the chemical composition of HW CMa a spectrum of the binary was obtained on UT 2008 February 26 with the FIES instrument on the 2.5 m Nordic Optical Telescope (La Palma). The Julian date at mid exposure is HJD 2 454 523.38203, corresponding to orbital phase 0.2469. The S/N ratio of this observation is

Table 5. Spectroscopic orbital solution for HW CMa.

Parameter	Value
Adjusted quantities:	
K_p (km s ⁻¹)	68.47 ± 0.23
K_s (km s ⁻¹)	66.18 ± 0.21
γ (km s ⁻¹)	+16.91 ± 0.10
e	0.5016 ± 0.0018
ω (°) ^a	86.38 ± 0.26
Adopted quantities:	
P (days)	21.1178329
T_1 (HJD-2 400 000) ^b	52279.6787
Derived quantities:	
$M_p \sin^3 i$ (M_\odot)	1.700 ± 0.011
$M_s \sin^3 i$ (M_\odot)	1.759 ± 0.012
$q \equiv M_p/M_s$	0.9665 ± 0.0043
$a_p \sin i$ (10 ⁶ km)	17.202 ± 0.055
$a_s \sin i$ (10 ⁶ km)	16.626 ± 0.050
$a \sin i$ (R_\odot)	48.63 ± 0.10
Other quantities pertaining to the fit:	
N_{obs}	48
Time span (days)	3759
σ_p (km s ⁻¹)	1.05
σ_s (km s ⁻¹)	0.95

^a Longitude of periastron for the less massive (primary) star.

^b Time of central primary eclipse (eclipse of the less massive star).

approximately 120 per pixel at a wavelength of 6160 Å. The reduction and analysis were carried out in the same way as described in Sect. 2.2. For the VWA analysis we selected only lines with measured equivalent widths smaller than 65 mÅ in the composite spectrum (corresponding to about 140 mÅ for the primary and 120 mÅ for the secondary), and we assumed a light ratio of $L_p/L_s = 0.90$ for the V band (see Sect. 3.4). The surface gravities of the components were both held fixed at a preliminary estimate of $\log g = 4.23$, near the final values in Sect. 3.4. The $v \sin i$ values were measured to be 12.0 ± 1.0 km s⁻¹ for both stars (for an adopted macroturbulent velocity of $\zeta_{RT} = 7$ km s⁻¹), although this has little impact on the abundance results. The temperatures yielding the best agreement between the abundances of Fe I and Fe II are 7500 K for the primary and 7700 K for the secondary, with uncertainties estimated at 150 K.

We tested a range of [Fe/H] values for the model atmospheres used in the VWA analysis, as well as different values of the microturbulence in order to examine the sensitivity of the results. The final [Fe/H] level of +0.30 dex for the model atmospheres was chosen to be consistent with that found below from the equivalent widths. Microturbulent velocities were 2.55 ± 0.80 km s⁻¹ for both stars. Individual elemental abundances for 16 species are presented in Table 6 on the scale of the solar abundances

Table 6. Abundances for the components of HW CMa.

Element	Primary			Secondary		
	[X/H]	σ	N	[X/H]	σ	N
C I	-0.66		1			
Na I	+0.34		1	+0.37		1
Mg I				-0.24		2
Si I	+0.02	0.09	6	+0.13	0.12	4
Si II	+0.40		1	+0.24		2
Ca I	-0.64	0.17	4	-0.65		2
Ti II	+0.25		2	+0.18	0.15	4
Cr I	+0.08		1	-0.31		1
Cr II	+0.57	0.18	3	+0.35	0.11	6
Fe I	+0.30	0.08	31	+0.29	0.08	24
Fe II	+0.37	0.09	12	+0.35	0.10	15
Ni I	+0.32	0.15	5	+0.52	0.09	12
Zn I	+0.28		1	+0.26		2
Sr II	+0.72		1	+0.10		1
Y II	+0.87		1	+0.75		1
Ba II	+1.14		2	+1.16	0.18	3

NOTE: These abundances are based on $v_{mic} = 2.55$ km s⁻¹ for both stars, and [Fe/H] = +0.30 for the model atmospheres applied in the analysis. Fe I abundances include corrections for NLTE. N represents the number of lines of each element, and σ is the scatter of the measurements (listed only if $N > 2$). The primary is the less massive star in the binary.

of Grevesse et al. (2007). An NLTE correction to Fe I of +0.06 dex for the primary and +0.07 dex for the secondary (Rentzsch-Holm 1996) is included. The average iron abundance is essentially identical for the two stars: [Fe/H] = $+0.33 \pm 0.15$ for the primary and $+0.32 \pm 0.15$ for the secondary (uncertainties include contributions from errors in T_{eff} and v_{mic}).

The abundance pattern for the components of HW CMa is shown graphically in Fig. 10. There are strong indications of the Am phenomenon in both stars: Ca seems characteristically deficient, along with C (at least in the primary), and heavier elements appear to be enhanced. In particular, Sr, Y, and Ba are generally much stronger than normal. The Fe/Ca difference is the same for both components (0.97 dex), and is considerably larger than we found for SW CMa. Additionally, for that system we measured Zn to be stronger than iron by a factor of 3–4 in both stars, while in HW CMa these two elements have about the same abundance. Scandium is a highly diagnostic element in Am stars, where it is usually found to be deficient. Unfortunately, however, no lines of this element are suitable for measurement in our spectra of either system. Nevertheless, the overall abundance pattern in both SW CMa and HW CMa is quite similar to that found in many other studies of Am stars (see, e.g., Okyudo & Sadakane 1990, Hui-Bon-Hoa 2000, Yushchenko et al. 2004, Iliev et al. 2006, Fossati et al. 2007, Gebran et al. 2008, 2010).

3.3. Photometric elements

The *uvby* differential photometry used for HW CMa is that reported by Clausen et al. (2008), obtained with the 0.5 m Strömgen Automatic Telescope at ESO (La Silla) between 1989 February and 2002 March. A total of 415 observations were obtained in each filter, with similar average uncertainties per differential measurement as for SW CMa (~ 5 mmag in *vby* and ~ 6 mmag in *u*). The system was observed intensively at the expected phase of secondary eclipse, but no significant drop in brightness was detected, as mentioned earlier. With only a single eclipse to constrain the geometry, this data set therefore poses special challenges to extract reliable orbital elements: the central surface brightness ratio J_s is completely unconstrained, there is no information in the light curve on the eccentricity ($e \cos \omega$), and the radius ratio k is very poorly defined without an external constraint.

As for the case of SW CMa, we used the JKTEBOP program for the light-curve solutions given that the stars are essentially spherical (oblateness ~ 0.00006). The ephemeris adopted is that of Sect. 3. The eccentricity and longitude of periastron were held fixed at the spectroscopic values, as was the mass ratio. In order to constrain J_s we calculated model spectra for each star from the MARCS series (Gustafsson et al. 2008) for the adopted temperatures (7560 K and 7700 K for the primary and secondary; see Sect. 3.4), and used them to obtain J_s estimates of 1.078 (*u*), 1.105 (*v*), 1.091 (*b*), 1.075 (*y*), and 1.081 (5187 Å), with only a small dependence on $[\text{Fe}/\text{H}]$ and $\log g$. The *y* value is nearly identical to that obtained from the empirical flux scale of Popper (1980), $J_s = 1.076$ in *V*, supporting the accuracy of the theoretical calculations.

Because of its sensitivity to k , the spectroscopic light ratio ($L_s/L_p \propto J_s k^2$) provides a very useful constraint on the poorly defined ratio of the radii in HW CMa. The average spectroscopic light ratio from three independent determinations described below in Sect. 3.4 is $L_p/L_s = 0.90 \pm 0.02$, or $L_s/L_p = 1.11 \pm 0.02$. This corresponds strictly to the mean wavelength of our spectroscopic observations (5187 Å). Light ratios in the Strömgen bands that are needed for the light curve fits were inferred by making an initial estimate of k requiring that the combination of the measured L_s/L_p and k match the theoretical value of J_s at 5187 Å. We then used this estimate of $k = 1.013$ along with the J_s values in *uvby* to obtain the corresponding light ratios: 1.106 (*u*), 1.134 (*v*), 1.119 (*b*), and 1.103 (*y*).

JKTEBOP fits were performed separately in each passband, fixing J_s and L_s/L_p to the values specified above and holding $e \sin \omega$ and $e \cos \omega$ fixed as well (from the spectroscopy). We solved for i , $r_p + r_s$, k , and the usual photometric scale factor and phase offset. Solutions were carried out using LD coefficients for the linear law from both the Claret (2000) and van Hamme (1993) tables. The geometric elements with each set of coefficients show good agreement between the *v*, *b*, and *y* bands, with *u* being

Table 7. Adopted photometric elements for HW CMa.

i ($^\circ$)	84.84 ± 0.06			
$r_p + r_s$	0.06769 ± 0.00066			
k	1.012 ± 0.013			
r_p	0.03365 ± 0.00037			
r_s	0.03404 ± 0.00042			
	<i>y</i>	<i>b</i>	<i>v</i>	<i>u</i>
J_s	1.075 ± 2	1.091 ± 2	1.105 ± 2	1.078 ± 2
L_s/L_p	1.100 ± 20	1.121 ± 20	1.135 ± 21	1.108 ± 20

NOTE: Flux ratios are based on the measured effective temperatures and MARCS models. Luminosity ratios are constrained to match the spectroscopic value at 5187 Å. The geometric elements are the weighted mean of the *vby* values from Table C.2 using linear limb-darkening coefficients from van Hamme (1993).

more discrepant (and also more uncertain). We describe the results of these tests in Appendix C (available electronically).

In previous papers of this series the LD coefficients from van Hamme (1993) have generally been found to be in better agreement than those from Claret (2000) with the values that result when the coefficients are left free in the solutions (which cannot be done here, for obvious reasons), and that was the case for SW CMa as well (see Appendix B). Consequently, for the final light elements of HW CMa we adopt the van Hamme (1993) coefficients, and take the weighted average of the *vby* solutions (excluding *u*). These values are presented in the top portion of Table 7, where the uncertainties include a contribution from the scatter between the different bandpasses. A final set of solutions was carried out in each passband with the geometric elements held fixed at these weighted average values, in order to derive the luminosity ratios. These are listed at the bottom of the table. The observations and fitted curves near the primary eclipse are shown in Fig. 11. The final fits indicate only 22% of the *y*-band light of the photometric primary (less massive star) is blocked at phase 0.0.

3.4. Absolute dimensions

The mass determinations for HW CMa are both good to about 0.7%. Despite the difficulties described in the preceding section, the radii are also very precise, with relative uncertainties of only 1.1% and 1.3% for the primary (less massive star) and secondary that we consider realistic. These and other properties of the system are collected in Table 8.

With the *uvby* indices out of eclipse from Clausen et al. (2008) and the calibration by Crawford (1979) we derive an estimate of the interstellar reddening toward

HW CMA of $E(b - y) = 0.026$. We assign to this a conservative uncertainty of 0.01 mag. The corresponding extinction is $A(V) = 0.11 \pm 0.04$. A rather similar value is obtained from the dust maps of Hakkila et al. (1997), which give $A(V) = 0.13$ or $E(b - y) = 0.031$ after correction for the distance to the binary. On the other hand, Schlegel et al. (1998) suggest larger values of $A(V) = 0.20$ and $E(b - y) = 0.049$. In the following we adopt the more reliable photometric estimate. Table 8 includes also the individual Strömgren indices of the components, derived from the combined *uvby* magnitudes and the light ratios used in our photometric solutions. After de-reddening, these lead to photometric temperatures of 7777 ± 102 K and 7972 ± 107 K using the calibration of Napiwotzki et al. (1993), in which the uncertainties include observational errors but not the unknown dispersion of the calibration.

Table 8. Astrophysical properties of the HW CMA system.

	Primary	Secondary
Absolute dimensions:		
$M (M_{\odot})$	1.721 ± 0.011	1.781 ± 0.012
$R (R_{\odot})$	1.643 ± 0.018	1.662 ± 0.021
$\log g$ (cgs)	4.242 ± 0.010	4.247 ± 0.011
$v \sin i$ (km s ⁻¹) ^a	12.0 ± 1.0	12.0 ± 1.0
v_{sync} (km s ⁻¹) ^b	3.9 ± 0.1	4.0 ± 0.1
v_{psync} (km s ⁻¹) ^c	11.1 ± 0.1	11.2 ± 0.2
v_{peri} (km s ⁻¹) ^d	13.7 ± 0.2	13.8 ± 0.2
Radiative and other properties:		
T_{eff} (K)	7560 ± 150	7700 ± 150
M_{bol} (mag)	2.488 ± 0.089	2.383 ± 0.088
$\log L/L_{\odot}$	0.898 ± 0.036	0.940 ± 0.035
BC_V (mag)	$+0.03 \pm 0.10$	$+0.03 \pm 0.10$
M_V (mag)	2.46 ± 0.13	2.35 ± 0.13
Distance (pc)	306 ± 15	
$V - M_V$ (mag)	7.43 ± 0.10	
[Fe/H] ^e	$+0.33 \pm 0.10$	$+0.28 \pm 0.10$
Photometric indices:		
V ^f	9.996 ± 0.012	9.892 ± 0.011
$(b - y)$ ^f	0.139 ± 0.005	0.118 ± 0.005
m_1 ^f	0.225 ± 0.011	0.231 ± 0.011
c_1 ^f	0.817 ± 0.016	0.858 ± 0.016
$E(b - y)$	0.026 ± 0.010	

^a Measured projected rotational velocity.

^b $v \sin i$ expected for synchronous rotation.

^c $v \sin i$ expected for pseudo-synchronous rotation.

^d Expected $v \sin i$ if synchronized at periastron.

^e Values representative of the surface layers only.

^f Not corrected for interstellar absorption/reddening.

NOTE: The bolometric corrections (BC_V) are adopted from Flower (1996), along with with $T_{\text{eff}\odot} = 5780$ K, and $M_{\text{bol}\odot} = 4.73$ (see Torres 2010). An additional error contribution of 0.10 mag is added in quadrature to the BC_V uncertainty propagated from the temperature uncertainties.

These estimates are 200–250 K hotter than the adopted spectroscopic values.

In addition to the two consistent estimates of the effective temperatures reported earlier from the CfA/DS and FIES spectra, we obtained another measure by disentangling the DS spectra and using a cross-correlation procedure similar to that described in Sect. 2.1 for SW CMA, but adapted for single-lined spectra. The disentangling was carried out with a revised version provided by E. Sturm of the original procedure introduced by Simon & Sturm (1994). The results are 7500 K and 7620 K for the primary and secondary.⁵ A further spectroscopic estimate of the temperatures was made from three spectra of HW CMA collected with the TRES instrument (Szentgyorgyi & Fűrész 2007) on the 1.5 m reflector at the F. L. Whipple Observatory ($\lambda/\Delta\lambda \approx 44\,000$, $\lambda\lambda 3900\text{--}8900$ Å). These observations were initially intended to support the abundance determinations in Sect. 3.2, but turned out to be too weak for that purpose. Application of the TODCOR-based cross-correlation procedures used before for composite spectra gave T_{eff} values of 7610 K and 7670 K for the primary and secondary, and a light ratio of $L_p/L_s = 0.89 \pm 0.02$ at a mean wavelength of 5187 Å. Finally, we applied the same TODCOR analysis technique to the FIES spectrum we used earlier for the abundance analysis, and obtained 7570 K and 7740 K along with an identical light ratio of 0.89 ± 0.02 . The above determinations are all in good agreement, and establish that the primary (less massive star) is slightly but significantly cooler than the secondary. We adopt a straight average of the five temperature estimates, 7560 K and 7700 K for the primary and secondary, to which we attach an uncertainty of 150 K. The corresponding spectral type is approximately A6. The average of the three independent spectroscopic light ratio determinations is $L_p/L_s = 0.90 \pm 0.02$.

The luminosities and distance were derived in the same way as for SW CMA. The system distance is 306 ± 15 pc. Nearly identical values of 307 ± 20 pc and 306 ± 20 pc obtained separately for the primary and secondary indicate excellent internal consistency. HW CMA and SW CMA are only 2'.5 apart on the sky and HW CMA is only half as distant as SW CMA, yet the reddening we find for HW CMA is slightly *larger*. This may indicate that interstellar extinction is patchy in this direction.

The measured projected rotational velocities for both components of HW CMA are consistent with the pseudo-synchronous velocities, assuming co-aligned orbital and spin axes (see Table 8).

⁵ While the cross-correlation technique applied to these disentangled spectra is able to extract a useful estimate of T_{eff} because it makes use of the full spectrum at once, there are not enough isolated lines of iron and other elements in this narrow wavelength region to attempt a detailed abundance analysis as was done earlier with the FIES spectrum.

4. Discussion

The following sections present a comparison of the measured properties for SW CMa and HW CMa against predictions from the theory of stellar evolution, stellar structure, and tidal evolution.

4.1. Stellar evolution

Accurate mass, radius, and effective temperature determinations, especially when accompanied by a measurement of the chemical composition, are among the most powerful constraints afforded by eclipsing binary stars to test models of stellar structure and evolution (see, e.g., Andersen 1991, Torres et al. 2010, and references therein). When these four quantities are available for both components in the system, there are essentially no free parameters in the comparison with publicly available models: to the extent that the measurements are accurate, the models will either be successful in reproducing all observations simultaneously within their errors, or they will fail.⁶

In the case of Am stars such as SW CMa and HW CMa, however, the measured abundances do not represent the bulk composition of the stars, which is the relevant quantity when comparing with models. Instead, they are only a reflection of local changes in the surface layers attributed to diffusion processes, which give the spectra of these objects their peculiar appearance. Metallicity therefore remains a free parameter when testing models for these stars. Nevertheless, because detailed abundance patterns in Am stars vary from case to case and are not yet completely understood, a comparison with models is still of considerable interest – even if less constraining – to establish the precise evolutionary state of the stars. Except for second-order effects due to limb darkening, absolute masses and radii are essentially independent of the theory being tested. For HW CMa, however, our light-curve solutions have had to make additional use of model atmospheres to constrain the geometry of the system, because of the lack of secondary eclipses. We point out, though, that those models were used only in a differential sense (to determine *ratios* of central surface fluxes or bandpass-specific luminosities), so in effect the dependence on theory is very weak.

In this section we compare the absolute dimensions of SW CMa and HW CMa with stellar evolution models from the Yonsei-Yale series (Yi et al. 2001; Demarque et al. 2004), which have been shown previously to match observations very well. We have chosen these models primarily because they are provided with software to interpolate evolutionary tracks (and isochrones) for any given mass

and metallicity, the mass being among the most accurately known properties for these stars.

The $\log g$ vs. T_{eff} diagram for SW CMa in Fig. 12 allows a simultaneous comparison of the models against the three key observables: M , R , and T_{eff} . Evolutionary tracks corresponding to a composition slightly above solar ($[\text{Fe}/\text{H}] = +0.05$, with no α -element enhancement) are shown for the exact masses we measure (Table 4), with the gray areas representing the uncertainty in the location of the tracks that comes from the mass errors (in this case, a small fraction of the mass difference). Isochrones are also displayed for ages 500–900 Myr, in steps of 100 Myr. The models for this composition provide a very good fit to the observations, within the uncertainties, and the age inferred is approximately 700 Myr (indicated with the thicker isochrone). SW CMa is seen to be somewhat evolved, and currently near the mid-point of its main sequence phase. The implied bulk composition inferred from theory, $[\text{Fe}/\text{H}] = +0.05$, is ~ 0.4 – 0.5 dex lower than the iron abundance measured at the surface ($[\text{Fe}/\text{H}] = +0.49/+0.61$ for the primary and secondary, respectively), which may be interpreted as giving a rough measure of the *true* enhancement of the iron-peak elements in the photospheres of these stars. Strictly speaking, however, this factor of three enhancement may only be a lower limit, as the effects of metallicity and α -element enhancement in the models can trade off against each other to some extent, leading to mass tracks and isochrones that fit the observations equally well. For example, a match as good as seen above is achieved also with $[\text{Fe}/\text{H}] = -0.10$ and $[\alpha/\text{Fe}] = +0.22$, with $[\text{Fe}/\text{H}] = -0.20$ and $[\alpha/\text{Fe}] = +0.36$, etc.

Separate diagrams of the radius and effective temperature as a function of mass are seen in Fig. 13, along with the same isochrones from the previous figure. The models provide a virtually exact match to the mass and radius of the components at 700 Myr, and a good fit to the temperatures as well.

Similar diagrams for HW CMa can be seen in Fig. 14 and Fig. 15. In this case, the model composition that best fits the observations is $[\text{Fe}/\text{H}] = +0.23$ (with $[\alpha/\text{Fe}] = 0.0$), and the implied age is approximately 160 Myr. Solar composition tracks are shown for reference as dotted lines in Fig. 14. HW CMa is essentially on the zero-age main sequence. To the extent that $[\text{Fe}/\text{H}] = +0.23$ represents the overall composition of this system, it would appear that the true enhancement of the iron-peak elements in the surface layers is a modest 0.1 dex in this case, since the measured photospheric abundances are $[\text{Fe}/\text{H}] = +0.33/+0.32$. As before, this conclusion is dependent on the assumed $[\alpha/\text{Fe}]$ enhancement, which is inaccessible to observation in both of these systems. The higher-than-solar bulk $[\text{Fe}/\text{H}] = +0.23$ composition for HW CMa suggested by the models is somewhat uncommon for stars in the solar neighborhood. If one enforces in the models a more typical solar-like iron abundance, the observations are about as well reproduced by increasing the $[\alpha/\text{Fe}]$ ratio to $+0.40$. This combination would imply a true surface-

⁶ Additional variables such as the helium abundance, mixing length parameter, convective core overshooting, etc., have generally already been chosen in advance by the modelers in published tables, and are not “tunable” by the user. Specific models for a particular system can of course be computed with different values of these additional variables, as we do in one example below, adding more freedom to the fits.

layer iron enhancement due to the Am phenomenon in HW CMa of ~ 0.3 dex, and the inferred age would be the same as before. However, a value of $[\alpha/\text{Fe}]$ as large as this is on the high side of the observed distribution for stars with solar iron abundance, which makes us somewhat skeptical of this scenario. Another possible way of reproducing the HW CMa observations with an iron composition closer to solar is to alter the helium abundance. Tests with the Granada models of Claret (2004) indicate, however, that the radii and effective temperatures can only be matched simultaneously with a very low helium abundance of $Y = 0.24$, at ages of 440–500 Myr that are significantly older than before. A helium abundance this close to the primordial value seems unlikely.

Comparisons (not shown) of the observations for HW CMa and SW CMa with the standard ($[\alpha/\text{Fe}] = 0.0$) Victoria-Regina stellar evolution models of Vandenberg et al. (2006) and with the Granada models of Claret (2004) give results that are quite consistent with those from the Yonsei-Yale models, indicating similar overall abundances and evolutionary ages.

4.2. Internal structure

The observed apsidal motion for SW CMa, $\dot{\omega} = 0.00067 \pm 0.00021$ deg cycle $^{-1}$ (Clausen et al. 2008), is a measure of the average degree of central mass concentration of the components. The corresponding average apsidal motion constant for the system is $\log k_{2,\text{obs}} = -2.57 \pm 0.30$. Using the absolute dimensions of the stars from Table 4, the models by Claret (2004) predict a theoretical value of $\log \bar{k}_{2,\text{theo}} = -2.582 \pm 0.050$, in which the formal uncertainty does not account for possible systematic errors in the models. While this is consistent with the empirical value within the errors, the close agreement may be accidental given the difficulty of the measurement (the apsidal period is long: $U = 14\,900 \pm 4\,700$ yr). The General relativistic contribution ($\dot{\omega}_{\text{GR}} = 0.00034$ deg cycle $^{-1}$) amounts to about 50% of the total apsidal motion.

While the eccentric system HW CMa is also expected to display apsidal motion, the lack of secondary minima precludes such a measurement based on eclipse timings. Spectroscopic detection of the effect would be quite challenging. The models of Claret (2004) predict a value of $\dot{\omega} = 0.00023$ deg cycle $^{-1}$, and a corresponding apsidal motion constant of $\log \bar{k}_{2,\text{theo}} = -2.410 \pm 0.050$. The estimated period of this effect is $U = 88\,900$ yr, six times longer than in SW CMa. In the case of HW CMa the relativistic contribution completely dominates, accounting for 97% of the total apsidal motion.

4.3. Tidal evolution

In addition to their binarity, Am stars typically display slow rotation compared to field stars of the same spectral type. The components of SW CMa and HW CMa are no exception. We noted earlier that while the primary of

SW CMa appears to be pseudo-synchronized with the orbital motion, the secondary is not, and rotates at only half the corresponding speed. This assumes the spin axes are parallel to the axis of the orbit, a condition that is almost universally taken for granted in binaries. Here we investigate whether synchronization is expected at all in these systems according to tidal theory, and if so, whether the situation for the secondary of SW CMa might be understood in terms of spin-orbit misalignment. We examine also the predicted evolution of the orbital eccentricity.

We have integrated the differential equations given by Hut (1981) for the time evolution of the semimajor axis (da/dt), the eccentricity (de/dt), the angular rotation rates of both components ($d\Omega_1/dt$, $d\Omega_2/dt$), and the angle between the plane of the orbit and the equator of each star ($d\phi_1/dt$, $d\phi_2/dt$). These six, coupled equations were integrated simultaneously using a 4th-order Runge-Kutta method, with the stellar properties interpolated at each time step from appropriate evolutionary tracks from Claret (2004). The turbulent dissipation timescale for the late evolutionary phases with convective envelopes was taken to be $(MR^2/L)^{1/3}$, where M , R , and L are the mass, radius, and luminosity of the star. For phases in which the envelopes are radiative (the most relevant here) the timescales adopted follow closely those in Eq. 17 and Eq. 18 by Claret & Cunha (1997).

The initial conditions are of course not known, so they are in effect free parameters of the model. For the orbital period and eccentricity we have adjusted the starting values so as to match P and e at the current evolutionary age of each system. Their time evolution for SW CMa is shown in Fig. 16a and Fig. 16b, in which the vertical dotted lines mark the current age of about 680 Myr ($\log \tau = 8.833$), according to the Granada models employed in this section. Based on these calculations the orbit is expected to circularize at an age of $\tau = 835$ Myr ($\log \tau = 8.921$) for this system.

The evolution of the angular rotation rate $\Omega = 2\pi/P_{\text{rot}}$ of each star in SW CMa is seen in Fig. 16c, where for convenience we have normalized it to the orbital rate, $\Omega_{\text{orb}} = 2\pi/P_{\text{orb}}$. We have no observational constraint on the rotation rates, so the initial values were arbitrarily set to $\Omega_1/\Omega_{\text{orb}} = \Omega_2/\Omega_{\text{orb}} = 6.0$, reasonable for A-type stars that usually rotate very rapidly (at least in the field). A dot-dashed line in this figure indicates the pseudo-synchronous rate at each age, and the horizontal dotted line is the current pseudo-synchronous rate. These calculations suggest that pseudo-synchronization for both stars in this system was reached early-on, at an age of roughly 100 Myr ($\log \tau = 8.0$). This would indeed appear to be the case for the primary of SW CMa, based on its measured $v \sin i$ value, but not for the secondary.

The degree of spin-orbit alignment is represented by the angle ϕ , but once again, we have no constraint on this quantity. Furthermore, the relation between ϕ and the orbital and rotational inclination angles i_{orb} and i_{rot} ,

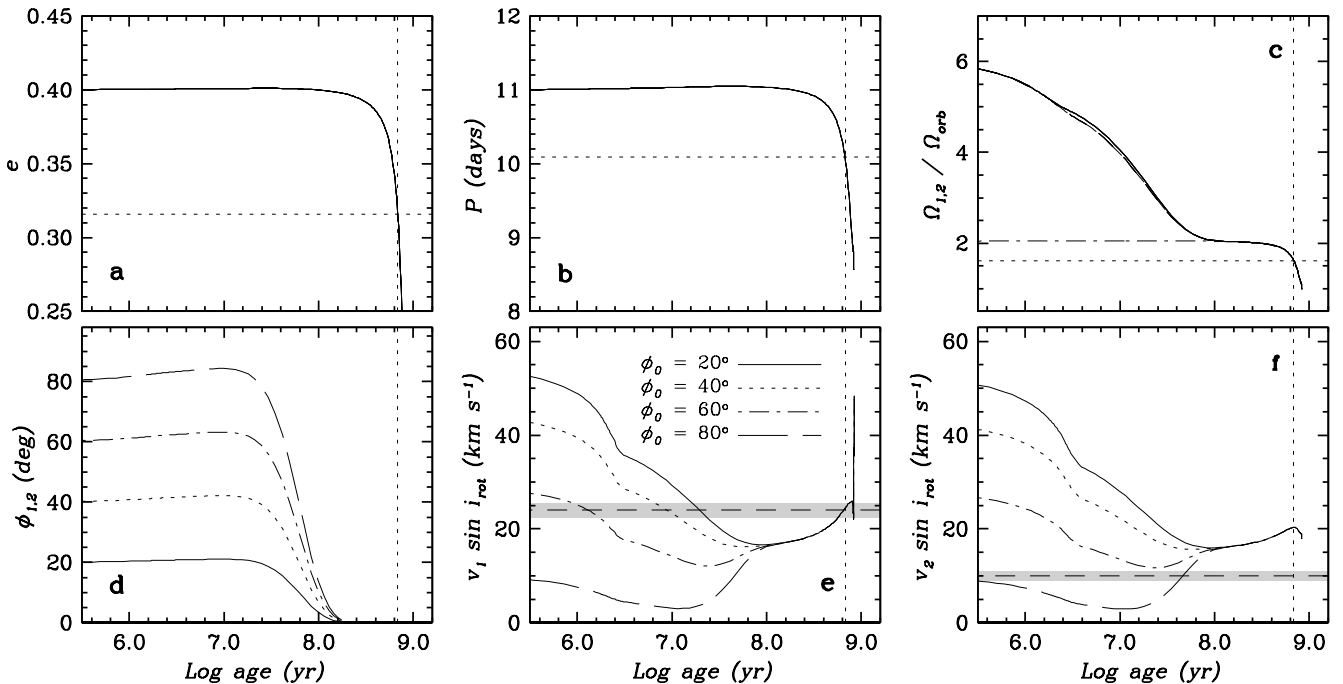


Fig. 16. Tidal evolution calculations for SW CMa, following the prescription by Hut (1981). The vertical dotted line in each panel represents the current evolutionary age of 680 Myr ($\log \tau = 8.833$), based on the models by Claret (2004). (a) Eccentricity as a function of time; (b) Orbital period; (c) Normalized angular rotation rate of each star. The dot-dashed line represents the evolution of the pseudo-synchronous value, and the horizontal dotted line is the pseudo-synchronous rate at the present age. (d) Angle between the equator of each star and the plane of the orbit. The four curves correspond to different initial values as given in the next panel. (e) Theoretical projected rotational velocity of the primary as a function of time, for four different initial values of the spin-orbit angle, ϕ_0 . The measured $v \sin i_{\text{rot}}$ and its uncertainty are indicated with the horizontal dashed line and shaded area. Theory agrees with observation at the current age of the system. (f) Same as (e), for the secondary. In this case theory is not able to match the observation, regardless of the initial values assumed for $\Omega/\Omega_{\text{orb}}$ and ϕ .

both measured with respect to the line of sight, is given by

$$\cos \phi = \cos i_{\text{orb}} \cos i_{\text{rot}} + \sin i_{\text{orb}} \sin i_{\text{rot}} \cos \lambda, \quad (1)$$

which involves an unknown angle λ between the sky-projected angular momentum vectors of the orbit and the stellar spin.

The spectroscopically measured projected rotational velocities of the stars, which we refer to more properly now as $v \sin i_{\text{rot}}$, do provide an indirect constraint on a combination of theoretically predictable quantities, but this still involves the unknown angle λ . Given that i_{orb} is rather close to 90° in both SW CMa and HW CMa we may make the approximation that $\cos \phi \approx \sin i_{\text{rot}} \cos \lambda$. We then have

$$v \sin i_{\text{rot}} \approx \frac{2\pi}{P_{\text{orb}}} \frac{\Omega}{\Omega_{\text{orb}}} \frac{\cos \phi}{\cos \lambda} R. \quad (2)$$

All quantities on the right-hand side of this equation are either known from stellar evolution calculations (R), or can be computed from the solution of the differential equations for tidal evolution, with the exception of the angle λ , which depends on the observer's viewpoint. In order to make progress, we ignore this term for the mo-

ment (or equivalently, we consider λ to be small), so that $\cos \phi \approx \sin i_{\text{rot}}$.

The evolution of the alignment angle ϕ for SW CMa is displayed in Fig. 16d for four different initial values (20° , 40° , 60° , 80°). The curves for the primary and secondary are nearly indistinguishable, so only those for the primary are shown. As seen from the convergence of the curves towards zero, spin-orbit alignment for both stars in SW CMa is reached at the age of about 200 Myr ($\log \tau \approx 8.3$), which is less than a third of the current age of the system. The predicted evolution of $v \sin i_{\text{rot}}$ for each star, computed from Eq. 2, is shown in Fig. 16e and Fig. 16f compared against the measured values (dashed line and shaded uncertainty region).

Independently of the initial values of ϕ and $\Omega/\Omega_{\text{orb}}$, the predictions from tidal evolution theory cannot be made to match the anomalously slow rotation rate of the secondary of SW CMa. The angle λ in Eq. 2 that we have previously ignored is inconsequential for this discussion, as any value greater than zero only makes the disagreement worse. Evidently current tidal theory is incomplete. An effect not considered here is the possible decoupling between the core of the star and the external layers, which suffer more directly the actions of tidal forces. Since the

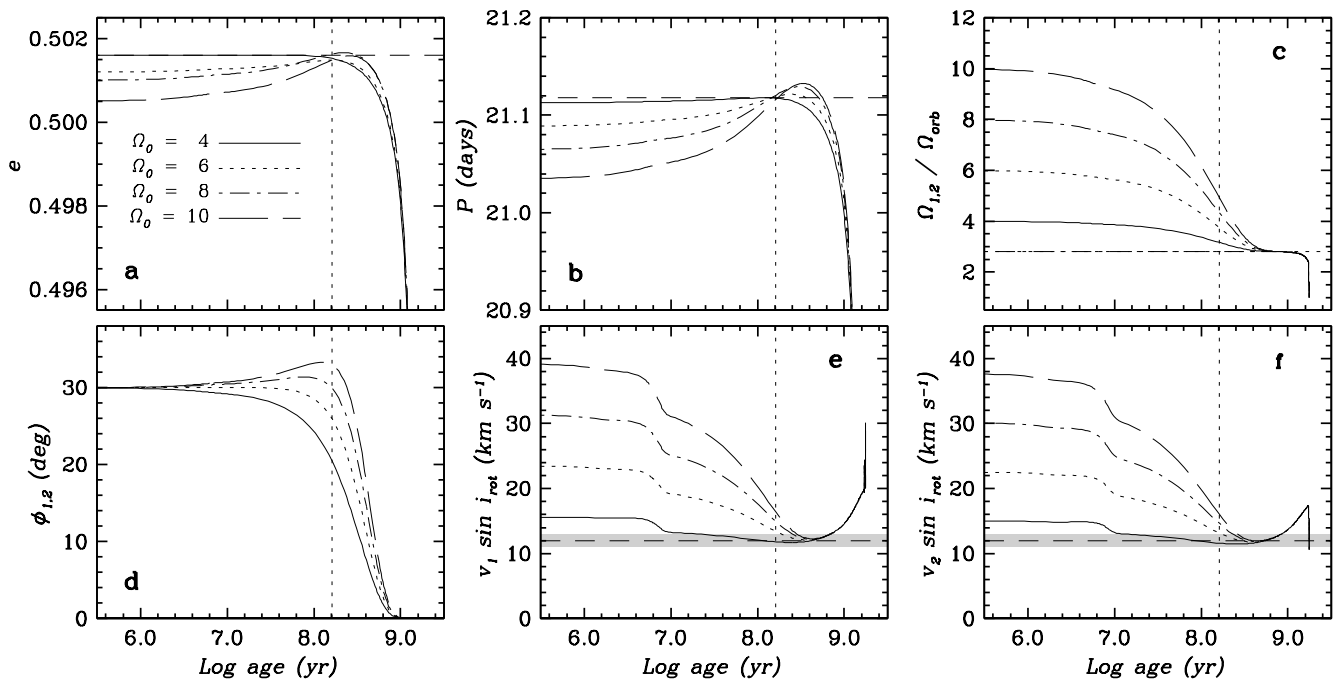


Fig. 17. Similar to Fig. 16, but for the HW CMA system. In this case the results are illustrated for four initial values of $\Omega/\Omega_{\text{orb}}$ (Ω_0 for short) as labeled in panel (a), and a single initial value for ϕ of 30° . With the boundary conditions tuned in this way, theory matches the measured rotational velocities of both components shown in (e) and (f). Neither star is predicted to be synchronized, and the calculations suggest their spin axes have not yet been aligned with the axis of the orbit.

spectroscopically measured $v \sin i_{\text{rot}}$ corresponds only to the layers that we see, it is quite possible that the larger rotation rate predicted by theory is more representative of a more rapidly rotating core than of the outer envelope, or at the very least is some average of the two, which would be larger than the measured value.

Similar tidal calculations for HW CMA are shown in Fig. 17. In this case we have chosen to illustrate the effects of a change in the initial values of $\Omega/\Omega_{\text{orb}}$, rather than ϕ . As before, we have adjusted the boundary conditions for the period and eccentricity to match the measured values at the current age, which is 160 Myr ($\log \tau = 8.21$) according to the Claret (2004) models. As the evolution of both of these quantities (Fig. 17a and Fig. 17b) depends on Ω (see Hut 1981), the starting values for P and e are different in each case. The calculations indicate that orbital circularization will occur at an age of ~ 1.75 Gyr ($\log \tau = 9.244$).

The time dependence of $\Omega/\Omega_{\text{orb}}$ appears in Fig. 17c, and influences the late evolution of the angle ϕ between the equator and orbital plane, as seen in Fig. 17d. These two panels indicate that neither star is expected to be pseudo-synchronized at the current age, nor has spin-orbit alignment been achieved. Pseudo-synchronization is predicted to happen at ~ 600 Myr ($\log \tau = 8.78$), and alignment at an age of approximately 1 Gyr. The fact that we do see agreement within the measurement errors between the observed rotational velocities and the predicted pseudo-synchronous velocities at the current epoch as listed in Table 8 suggests that this may be due to a

combination of non-synchronized angular rotation rates ($\Omega_{1,2}$) and slightly misaligned spin axes ($\phi_{1,2} \approx 20^\circ$ at the current epoch for our particular choice of the initial values for $\Omega_{1,2}$; see Fig. 17d). The theoretical projected rotational velocities are plotted in Fig. 17e and Fig. 17f. The lower curves match the measured $v \sin i_{\text{rot}}$ of each star at the current age, and correspond to initial $\Omega/\Omega_{\text{orb}}$ values of 4.0 for both stars, and initial angles $\phi_{1,2} = 30^\circ$ tuned to produce the agreement.

The asynchronous rotation of the secondary of SW CMA is not unusual for Am stars, or for normal A stars for that matter. The compilation of Torres et al. (2010) includes several such systems with well determined properties that show the same lack of synchronization. An extreme case is V459 Cas (Lacy 2004), a pair of A1m stars both rotating 3.5–4.5 times faster than pseudo-synchronous. There is no obvious correlation that we can see between asynchronous rotation and other global properties of Am or normal A stars. This issue has also been studied by others (Budaj 1996, 1997; Iliev et al. 2006; Prieur et al. 2006), but no credible pattern has emerged.

5. Final remarks

SW CMA and HW CMA join the very small ranks of Am stars with accurately known absolute dimensions (better than 2% relative errors in M and R) that also have their detailed abundances determined, in this case for a dozen or more elements in each star. We find that the measured masses, radii, and temperatures are well matched by stel-

lar evolution models such as those by Yi et al. (2001), with inferred bulk abundances of $[\text{Fe}/\text{H}] = +0.05$ and $+0.23$ and ages of ~ 700 and ~ 160 Myr, respectively. These abundances are 0.4–0.5 dex and 0.1 dex lower than those measured in the outer layers. These two systems seem to confirm previous evidence that the properties of Am stars are generally matched by stellar evolution models just as well as those of normal A stars, suggesting their properties are not fundamentally different, even though their surface abundances are. There are exceptions to this rule, though, such as the recently studied Am system of XY Cet (Southworth et al. 2011), whose stars do not seem to agree well with theory.

Internal structure models predict that apsidal motion in both SW CMa and HW CMa (empirically determined only in the first case) should be dominated by General relativistic effects ($\sim 50\%$ and 97% contributions, respectively). Current tidal theory suggests that the angular rotation rates of the SW CMa stars should be pseudo-synchronized with the orbital motion by now, and that their spin axes should be parallel to the orbital axis. Indeed we find that the measured projected rotational velocity of the primary agrees with expectations, but the measured $v \sin i$ of the secondary is too small by a factor of two, even though its mass is only 6% smaller than the primary. This disagreement cannot be resolved by tuning free parameters in the models, and underscores our incomplete understanding of these processes. For HW CMa theory predicts that neither pseudo-synchronization nor spin-orbit alignment have yet been reached. However, the measured rotations do agree with the pseudo-synchronous values in this case, which can nevertheless be explained with a proper combination of initial values for $\Omega/\Omega_{\text{orb}}$ and the spin-orbit alignment angle ϕ .

Acknowledgements. We dedicate this work to our long-time friend and colleague Jens Viggo Clausen, who passed away as this paper was being prepared for submission. He was a key participant in this series of articles, and will be remembered for his high standards, dedication, and careful attention to detail. Many of the spectroscopic observations at CfA were obtained by P. Berlind, J. Caruso, R. Davis, E. Horine, A. Milone, and J. Zajac. We are grateful to E. Sturm for providing his original disentangling code, and to him and J. D. Pritchard for modifying it for use on Linux/Unix computer systems. The anonymous referee is also thanked for a number of helpful comments. The projects “Stellar structure and evolution – new challenges from ground and space observations” and “Stars: Central engines of the evolution of the Universe”, carried out at Copenhagen University and Aarhus University, are supported by the Danish National Science Research Council. G.T. acknowledges partial support from NSF grant AST-1007992. The following internet-based resources were used in the research for this paper: the NASA Astrophysics Data System, the SIMBAD database and the VizieR service operated by CDS, Strasbourg, France, and the arXiv scientific paper preprint service operated by Cornell University.

References

- Abt, H. A. 1961, *AJ*, 66, 277
 Abt, H. A. 2000, *ApJ*, 544, 933
 Abt, H. A., & Morrell, N. I. 1995, *ApJS*, 99, 135
 Andersen, J. 1991, *A&A Rev.* 3, 91
 Böhm-Vitense, E. 2006, *PASP*, 118, 419
 Bruntt, H. 2009, *A&A*, 506, 235
 Bruntt, H., Bikmaev, I. F., Catala, C. et al. 2004, *A&A*, 425, 683
 Bruntt, H., De Cat, P., & Aerts, C. 2008, *A&A*, 478, 487
 Budaj, J. 1996, *A&A*, 313, 523
 Budaj, J. 1997, *A&A*, 326, 655
 Claret, A. 2000, *A&A*, 363, 1081
 Claret, A. 2004, *A&A*, 424, 919
 Claret, A., & Cunha, N. C. S. 1997, *A&A*, 318, 187
 Clausen, J. V., Vaz, L. P. R., García, J. M. et al. 2008, *A&A*, 487, 1081
 Crawford, D. L. 1979, *AJ*, 84, 1858
 Demarque, P., Woo, J.-H., Kim, Y.-C., & Yi, S. K. 2004, *ApJS*, 155, 667
 Etzel P. B. 1981, in *Photometric and Spectroscopic Binary Systems*, eds. E. B. Carling and Z. Kopal (Dordrecht: Reidel), 111
 Fekel, F. C., Williamson, M., Buggs, C., Onuoha, G., & Smith, B. 2006, *AJ*, 132, 1490
 Flower, P. J. 1996, *ApJ*, 469, 355
 Fossati et al. 2007, *A&A*, 476, 911
 Fossati et al. 2008, *A&A*, 483, 891
 Frandsen, S., & Lindberg, B. 1999, in *Astrophysics with the NOT*, ed. H. Karttunen & V. Pirola (Piikkio: Univ. Turku), 71
 Gebran, M., & Monier, R. 2008, *A&A*, 483, 567
 Gebran, M., Vick, M., Monier, R., & Fossati, L. 2010, *A&A*, 523, 71
 Gray, D. F. 2005, *The Observation and Analysis of Stellar Photospheres*, 3rd Edition, (Cambridge: Cambridge Univ. Press), 442
 Grevesse, N., Asplund, M., & Sauval, A. J. 2007, *Space Sci. Rev.* 130, 105
 Gustafsson, B., Edvardsson, B., Eriksson, K. et al. 2008, *A&A*, 486, 951
 Hakkila, J., Myers, J. M., Stidham, B. J., & Hartmann, D. H. 1997, *AJ*, 114, 2043
 Hoffmeister, C. 1932, *Astron. Nachr.*, 242, 131
 Hui-Bon-Hoa, A. 2000, *A&AS*, 144, 203
 Hut, P. 1981, *A&A*, 99, 126
 Iliev, I. K., Budaj, J., Feňovčík, M., Stateva, I., & Richards, M. T. 2006, *MNRAS*, 370, 819
 Kupka, F., Piskunov, N., Ryabchikova, T. A., Stempels, H. C., & Weiss, W. 1999, *A&AS* 138, 119
 Lacy, C. H. S. 1997, *AJ*, 113, 2226
 Lacy, C. H. S., Claret, A., & Sabby, J. A. 2004, *AJ*, 128, 1340
 Latham, D. W. 1992, in *IAU Coll. 135, Complementary Approaches to Double and Multiple Star Research*, ASP Conf. Ser. 32, eds. H. A. McAlister & W. I. Hartkopf (San Francisco: ASP), 110
 Latham, D. W., Nordström, B., Andersen, J. et al. 1996, *A&A*, 314, 864
 Latham, D. W., Stefanik, R. P., Torres, G. et al. 2002, *AJ*, 124, 1144
 Liu, Q., Andersen, J., Clausen, J. V., Nordström, B., & Stefanik, R. P. 1992, *IBVS No.* 3813

- Lyubimkov, L. S., Rachkovskaya, T. M., & Rostopchink, S. I. 1996, *Astr. Rep.*, 40, 802
- Martynov D. Ya. 1973, in *Eclipsing Variable Stars*, ed. V. P. Tsesevich, Israel Program for Scientific Translation, Jerusalem, p. 146
- Napiwotzki R., Schönberner D., & Wenske V. 1993, *A&A*, 268, 653
- Nelson B., & Davis W. 1972, *ApJ*, 174, 617
- Netopil, M., Paunzen, E., Maitzen, H. M., North, P., & Hubrig, S. 2008, *A&A*, 491, 545
- Nordström, B., Latham, D. W., Morse, J. A., et al. 1994, *A&A*, 287, 338
- Okyudo, M., & Sadakane, K. 1990, *PASJ*, 42, 317
- Popper, D. M. 1980, *ARA&A*, 18, 115
- Popper, D. M., & Etzel, P. B. 1981, *AJ*, 86, 102
- Prieur, J.-L., Carquillat, J.-M., & Imbert, M. 2006, *MNRAS*, 372, 703
- Rentzsch-Holm, I. 1996, *A&A*, 312, 966
- Schlegel, D. J., Finkbeiner, D. P., & Davis, M. 1998, *ApJ*, 500, 525
- Simon, K. P., & Sturm, E. 1994, *A&A*, 1994, 281
- Southworth, J., Maxted, P. F. L., & Smalley, B. 2004a, *MNRAS*, 351, 1277
- Southworth, J., Pavlovski, K., Tamajo, E. et al. 2011, *MNRAS*, 414, 3740
- Southworth, J., Zucker, S., Maxted, P. F. L., & Smalley, B. 2004b, *MNRAS*, 355, 986
- Szentgyorgyi, A. H., & Fűrész, G. 2007, *Rev. Mex. A&A*, 28, 129
- Torres, G. 2010, *AJ*, 140, 1158
- Torres, G., Andersen, J., & Giménez, A. 2010, *A&ARv*, 18, 67
- Torres, G., Lacy, C. H. S., Claret, A., & Sabby, J. 2000, *AJ*, 120, 3226
- Torres, G., Neuhäuser, R., & Guenther, E. W. 2002, *AJ*, 123, 1701
- Torres, G., Stefanik, R. P., Andersen, J. et al. 1997, *AJ*, 114, 2764
- Valenti, J., & Piskunov, N. 1996, *A&AS* 118, 595
- VandenBerg, D. A., Bergbusch, P. A., & Dowler, P. D. 2006, *ApJS*, 162, 375
- van Hamme, W. 1993, *AJ*, 106, 2096
- Vick, M., Michaud, G., Richer, J., & Richard, O. 2010, *A&A*, 521, A62
- Wallace, L., Hinkle, K., & Livingston, W. 1998, *An atlas of the spectrum of the solar photosphere from 13,500 to 28,000 cm⁻¹ (3570 to 7405 Å)*, (Tucson: National Optical Astronomy Observatories)
- Wolf, G. W., & Kern, J. T. 1983, *ApJS*, 52, 429
- Yi, S. K., Demarque, P., Kim, Y.-C. et al. 2001, *ApJS*, 136, 417
- Yushchenko, A. V., Gopka, V. F., Khokhlova, V. L., Lambert, D. L., Kim, C., & Kang, Y. W. 2004, *A&A*, 425, 171
- Zucker, S., & Mazeh, T. 1994, *ApJ*, 420, 806

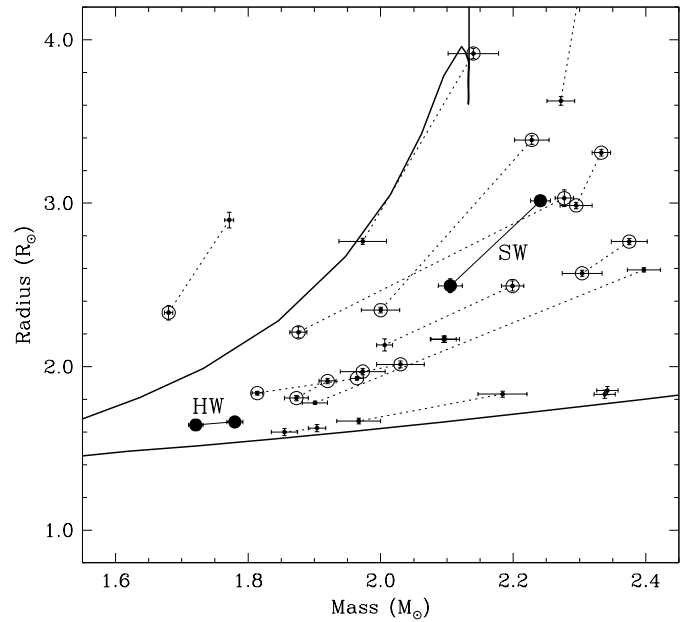


Fig. 1. Main sequence eclipsing binaries taken from Torres et al. (2010) in which both components have masses in the range 1.6–2.4 M_{\odot} , and relative errors in the masses and radii of 3% or better. Primary and secondary components are connected with dotted lines, and stars that are confirmed or probable Am stars are marked with open circles. SW CMa and HW CMa are shown with filled symbols. The thick solid lines are drawn for reference, and correspond to solar-metallicity isochrones from the series of Yi et al. (2001) for ages of 50 Myr and 1 Gyr.

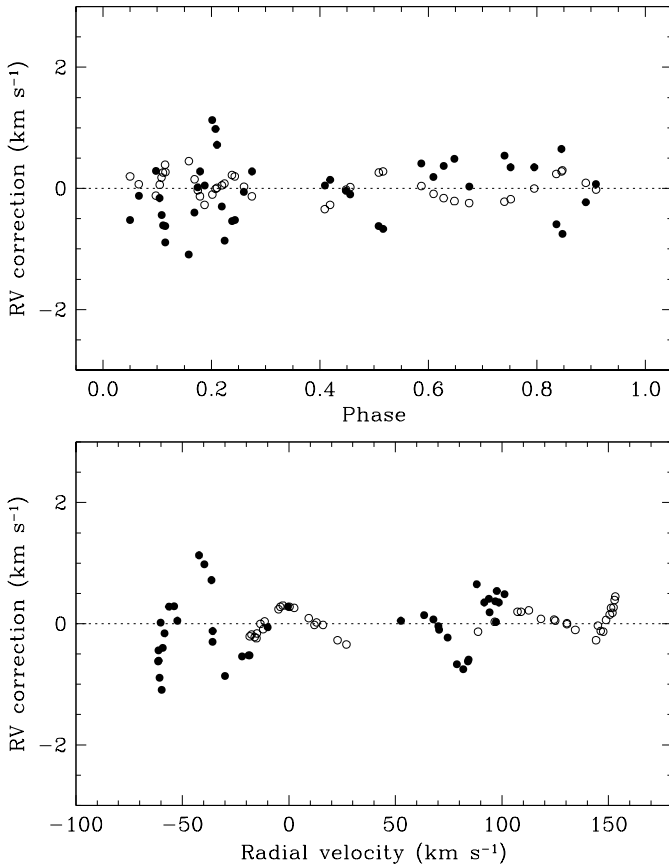


Fig. 2. Systematic errors to the raw TODCOR velocities of SW CMA determined from simulations based on synthetic binary spectra. Filled circles correspond to the primary, and open circles to the secondary. The velocity differences are shown as a function of orbital phase and radial velocity, and have been applied to the raw velocities as corrections. Phase 0.0 corresponds to the primary eclipse.

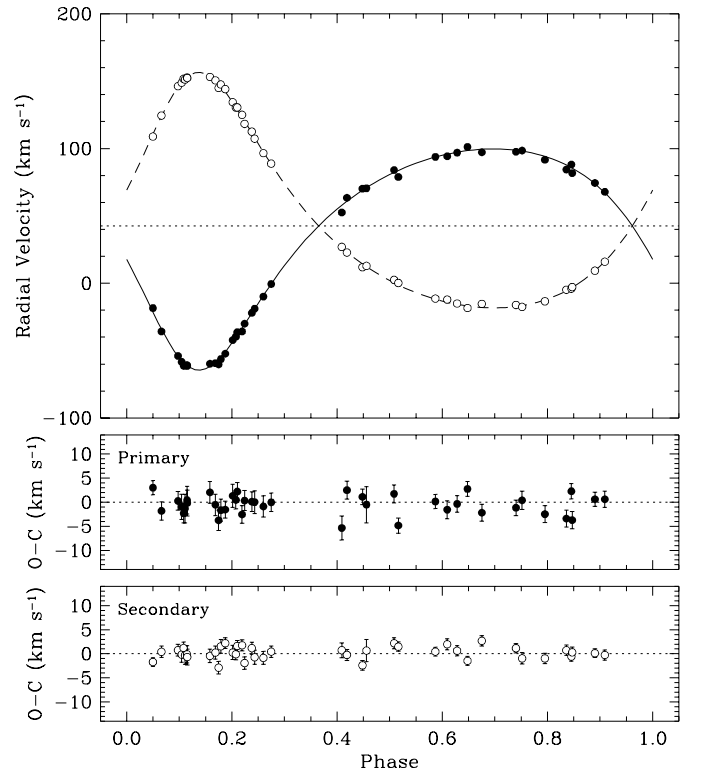


Fig. 3. Measured radial velocities for SW CMA and orbital solution (solid line for the primary, dashed for the secondary). The dotted line in the top panel indicates the center-of-mass velocity of the binary, and phase 0.0 corresponds to the primary eclipse. Residuals are shown at the bottom.

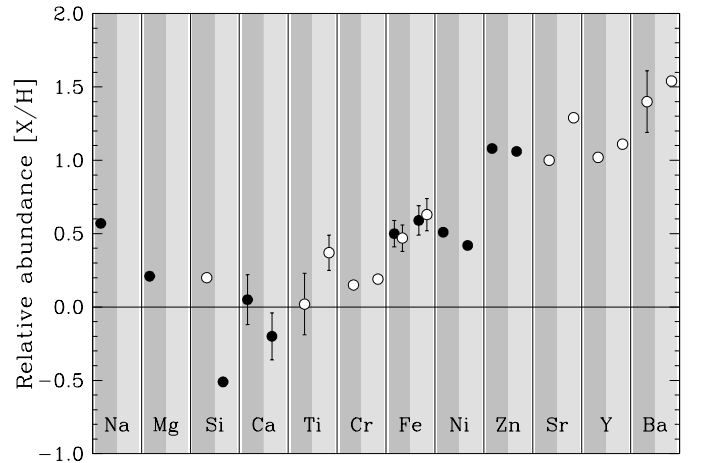


Fig. 4. Elemental abundances measured for SW CMA. Dark gray areas correspond to the primary, and light gray to the secondary. Filled and open symbols represent neutral and ionized species, respectively.

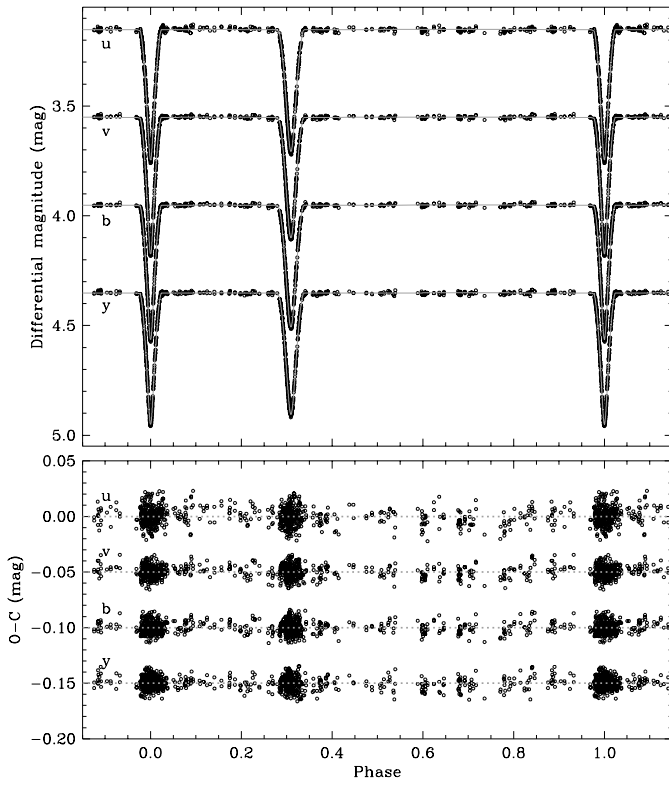


Fig. 5. *uvby* photometry for SW CMa together with our best fit models (Table 3). Phase 0.0 corresponds to the eclipse of the more massive star (primary eclipse). Residuals are shown at the bottom.

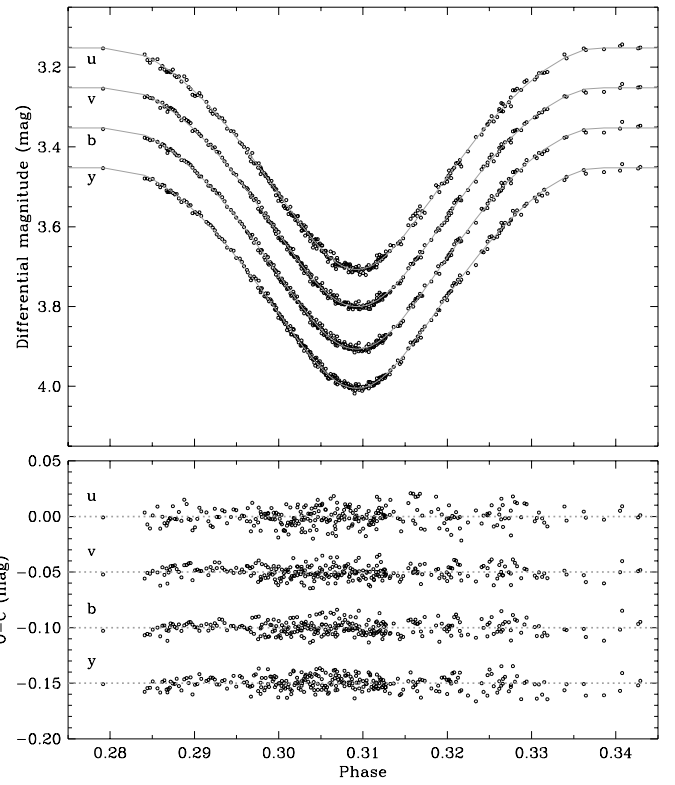


Fig. 7. Enlarged view of Fig. 5 around the secondary minimum of SW CMa.

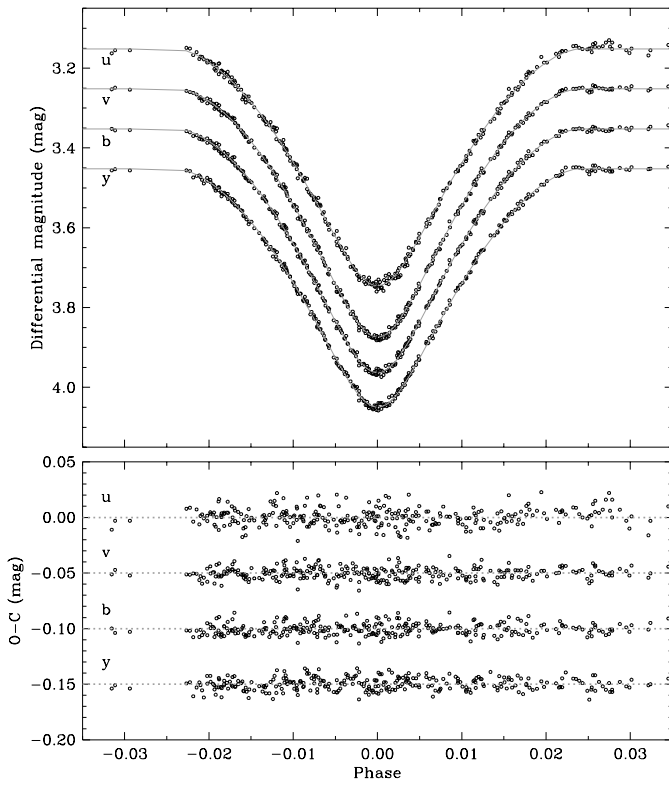


Fig. 6. Enlarged view of Fig. 5 around the primary minimum of SW CMa.

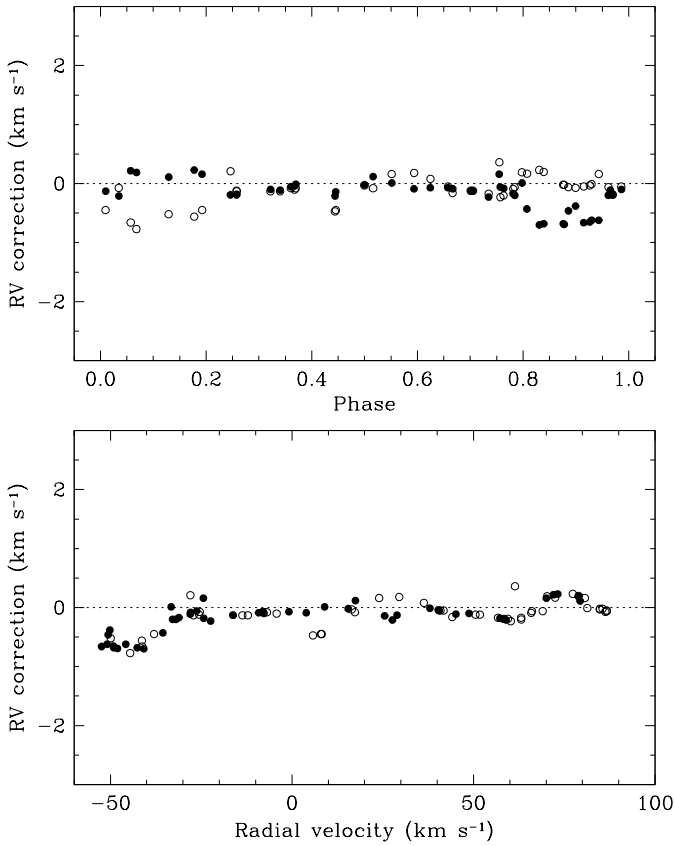


Fig. 8. Systematic errors in the raw TODCOR velocities of HW CMA determined from simulations based on synthetic binary spectra. Filled circles correspond to the more massive star, and open circles to the other component. The velocity differences are shown as a function of orbital phase and radial velocity, and have been applied to the raw velocities as corrections. Phase 0.0 corresponds to the eclipse of the less massive star.

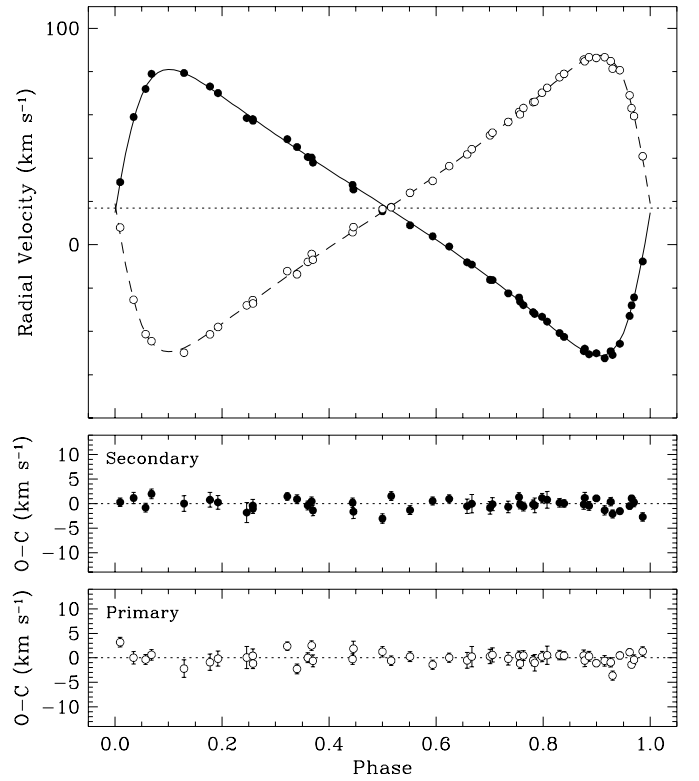


Fig. 9. Measured radial velocities for HW CMA and orbital solution (solid line for the more massive ‘secondary’ star, dashed for the primary). The dotted line in the top panel indicates the center-of-mass velocity of the binary, and phase 0.0 corresponds to eclipse of the less massive component. Residuals are shown at the bottom.

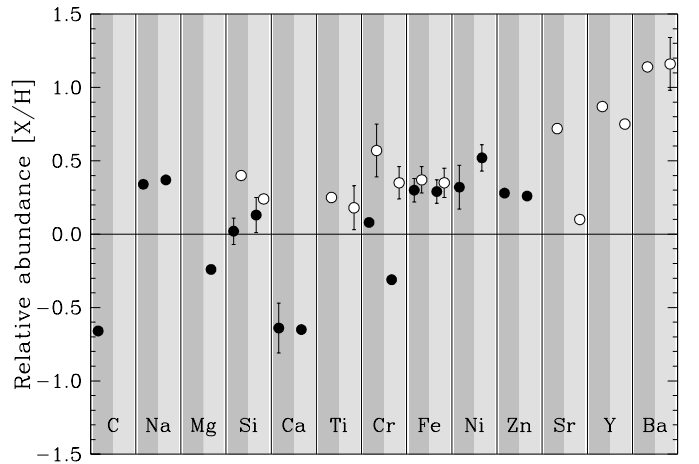


Fig. 10. Elemental abundances measured for HW CMA. Dark gray areas correspond to the primary (less massive star), and light gray to the secondary. Filled and open symbols represent neutral and ionized species, respectively.

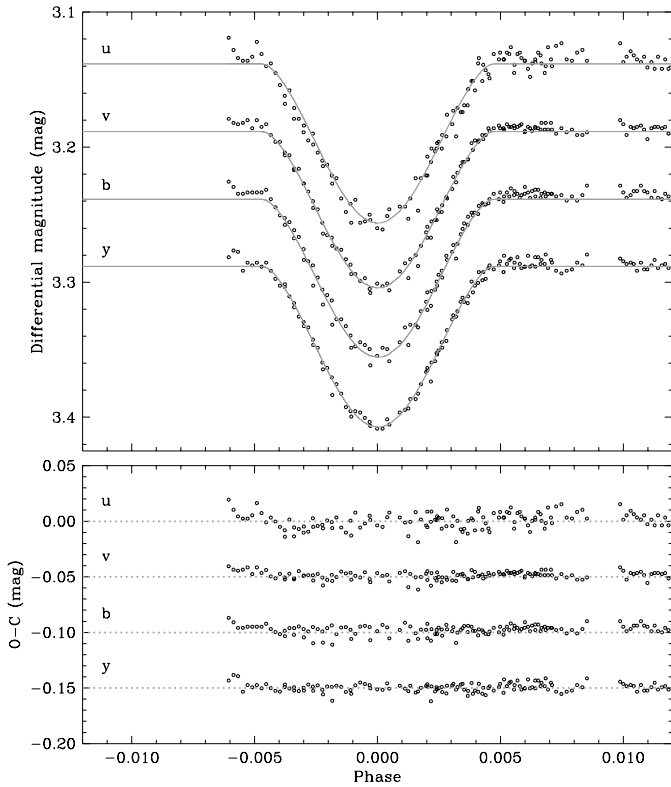


Fig. 11. *uvby* photometry for HW CMa near the primary minimum, together with our best fit models (Table 7). Residuals are shown at the bottom.

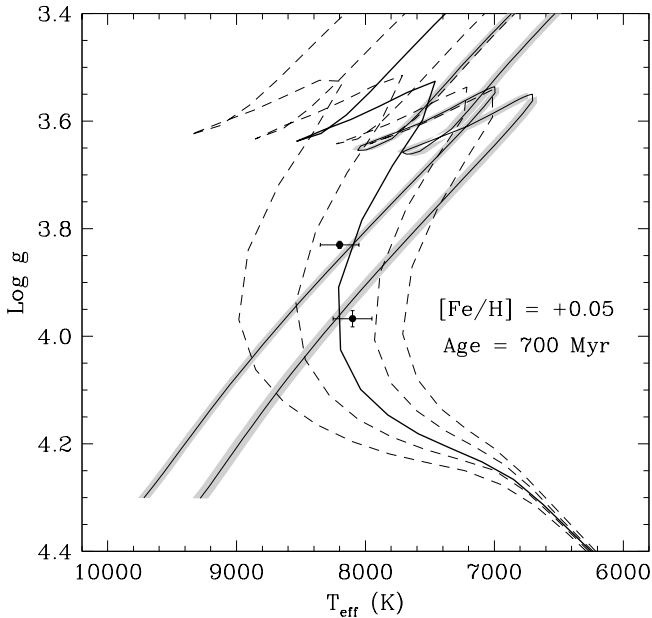


Fig. 12. Measurements for SW CMa compared against Yonsei-Yale models by Yi et al. (2001) for $[\text{Fe}/\text{H}] = +0.05$ and $[\alpha/\text{Fe}] = 0.0$. Evolutionary tracks for the measured masses are shown with solid lines and shaded areas indicating the uncertainty in the location of each track coming from the mass errors. Isochrones from 500 Myr to 900 Myr in steps of 100 Myr are represented by the dashed lines. The best fitting 700 Myr isochrone is drawn with a thicker line.

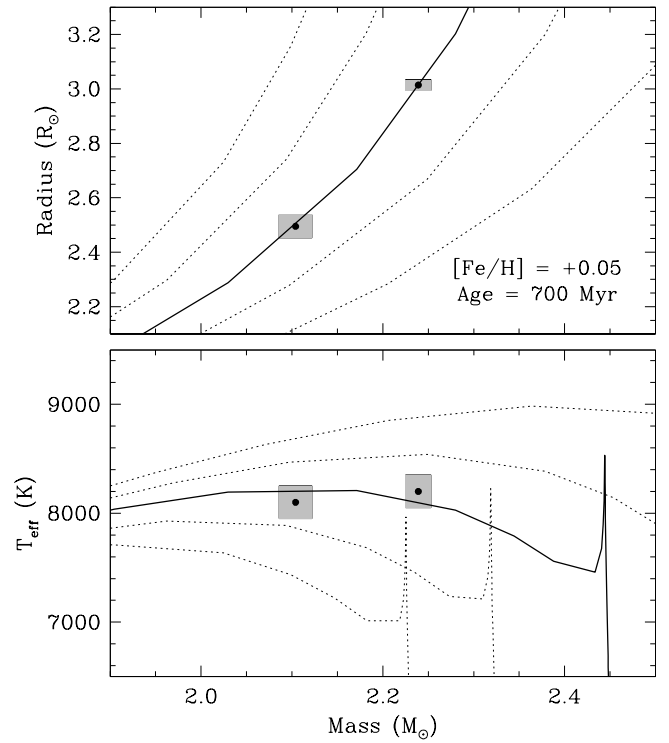


Fig. 13. Effective temperatures and radii for SW CMa shown as a function of the measured mass, with the observational errors represented by the shaded boxes. They are compared against $[\text{Fe}/\text{H}] = +0.05$ Yonsei-Yale isochrones by Yi et al. (2001) from 500 Myr to 900 Myr, in steps of 100 Myr, with $[\alpha/\text{Fe}] = 0.0$. The best-fitting model is indicated with a heavier line.

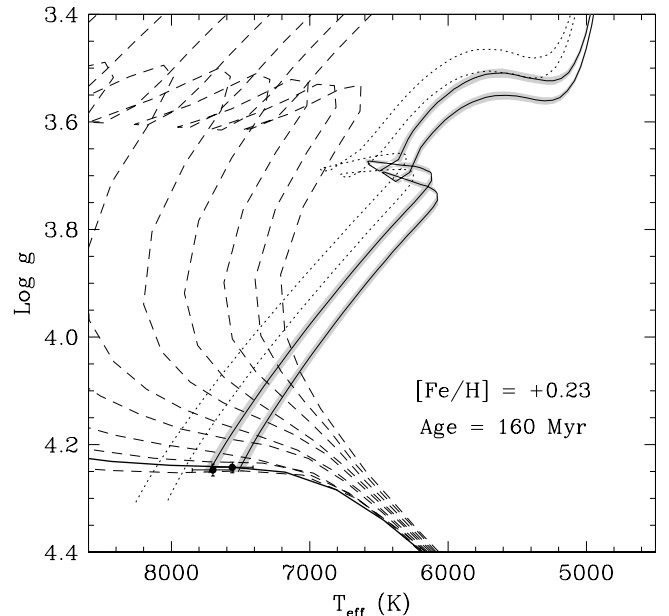


Fig. 14. Similar to Fig. 12, but for HW CMa. The best-fitting metallicity is $[\text{Fe}/\text{H}] = +0.23$. Solar metallicity tracks are shown for reference (dotted lines). The dashed lines represent Yonsei-Yale isochrones from 100 Myr to 1 Gyr in steps of 100 Myr. The best fitting 160 Myr isochrone is drawn with a thick solid line.

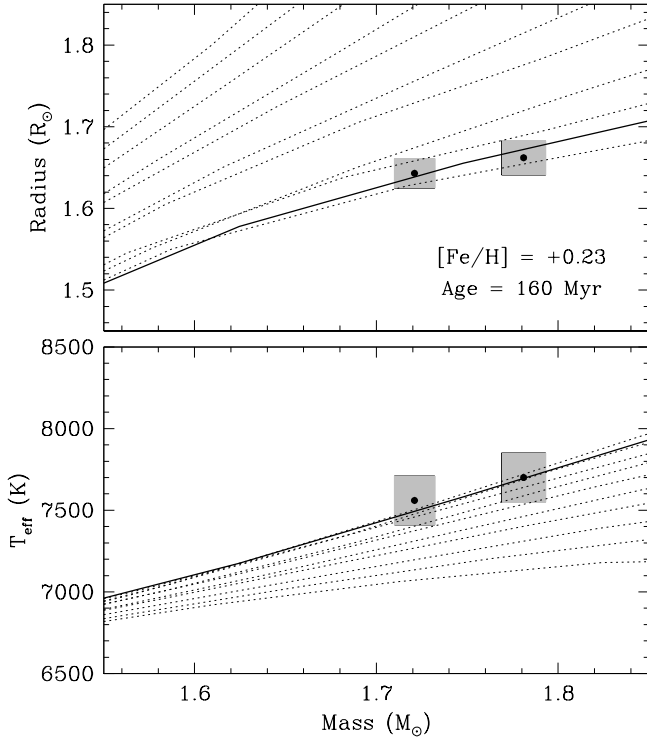


Fig. 15. Similar to Fig. 13, but for HW CMa. In this case the best-fitting metallicity is $[\text{Fe}/\text{H}] = +0.23$. The dotted lines represent Yonsei-Yale isochrones from 100 Myr to 1 Gyr in steps of 100 Myr. The best fitting 160 Myr model is drawn with a heavier solid line.

Table A.1. Radial velocities for SW CMa (with all corrections applied) and residuals from the final spectroscopic orbit.

HJD 2 400 000+	Phase	RV_p (km s ⁻¹)	RV_s (km s ⁻¹)	σ_p (km s ⁻¹)	σ_s (km s ⁻¹)	$(O - C)_p$ (km s ⁻¹)	$(O - C)_s$ (km s ⁻¹)
47254.6732	0.1151	-61.37	152.33	1.47	0.90	-0.17	-0.68
47461.8907	0.6480	101.18	-18.34	1.90	1.17	2.75	-1.45
47462.8217	0.7402	97.60	-16.08	1.93	1.19	-1.15	1.15
47463.7887	0.8360	84.37	-4.81	2.60	1.60	-3.40	0.73
47481.8766	0.6283	96.92	-15.02	2.00	1.23	-0.35	0.63
47487.7501	0.2103	-36.35	130.52	2.98	1.84	2.21	1.61
47487.8417	0.2194	-35.79	125.03	2.89	1.78	-2.53	1.76
47487.8904	0.2242	-30.05	118.29	2.70	1.66	0.34	-1.93
47489.7549	0.4090	52.54	26.98	2.23	1.38	-5.36	0.73
47489.8541	0.4188	63.41	22.83	2.21	1.36	2.50	-0.22
47490.7585	0.5084	84.03	2.51	2.12	1.31	1.74	2.21
47490.8401	0.5165	78.89	0.23	2.29	1.41	-4.85	1.49
47491.7770	0.6094	94.25	-12.11	1.78	1.10	-1.56	1.99
47494.8024	0.9091	67.85	16.06	2.38	1.47	0.61	-0.25
47497.7536	0.2016	-42.16	134.42	1.87	1.15	1.33	0.26
47497.8143	0.2076	-39.65	130.50	1.86	1.15	0.48	-0.08
47511.7356	0.5870	93.81	-11.36	1.83	1.13	0.15	0.45
47513.8367	0.7952	91.70	-13.33	2.09	1.29	-2.49	-0.96
47514.7963	0.8903	74.47	9.37	2.03	1.25	0.60	0.12
47517.7110	0.1791	-56.28	147.56	2.38	1.47	-1.66	1.55
47517.7960	0.1875	-52.30	144.11	2.21	1.36	-1.53	2.21
47518.6764	0.2748	-0.51	88.84	1.93	1.19	-0.02	0.45
47522.7188	0.6753	97.25	-15.26	2.48	1.53	-2.19	2.70
47526.6630	0.0662	-35.77	124.44	1.86	1.15	-1.80	0.42
47527.6974	0.1687	-59.26	150.60	1.61	0.99	-0.55	0.25
47527.7595	0.1748	-60.16	145.03	3.77	2.32	-3.75	-2.88
47538.7108	0.2600	-9.90	96.62	1.85	1.14	-0.88	-0.85
47540.6888	0.4559	70.50	12.97	1.58	0.97	-0.51	0.67
47543.6743	0.7518	98.52	-17.52	1.47	0.91	0.39	-0.95
47544.6361	0.8471	81.77	-2.82	1.86	1.15	-3.72	0.29
47546.6844	0.0500	-18.42	108.97	1.72	1.06	3.01	-1.71
47547.7765	0.1583	-59.76	153.21	1.53	0.94	2.05	-0.44
47548.6348	0.2433	-18.90	107.30	1.75	1.08	0.02	-0.71
47550.7033	0.4483	70.18	11.96	1.61	0.99	1.11	-2.40
47554.7119	0.8455	88.11	-4.06	1.91	1.18	2.28	-0.58
47558.6735	0.2380	-22.00	112.56	1.75	1.08	0.10	1.17
47577.5485	0.1083	-61.22	151.79	1.73	1.07	-2.30	1.21
47577.5732	0.1108	-61.14	151.22	1.59	0.98	-1.33	-0.31
47577.6135	0.1148	-60.68	152.79	1.78	1.10	0.42	-0.11
47587.5326	0.0976	-53.93	146.30	1.46	0.90	0.27	0.75
47587.6020	0.1045	-58.35	148.81	1.68	1.04	-0.96	-0.14

Appendix A: Radial velocity measurements

Table A.2. Radial velocities for HW CMa (with all corrections applied) and residuals from the final spectroscopic orbit.

HJD 2 400 000+	Phase	RV_s (km s ⁻¹)	RV_p (km s ⁻¹)	σ_s (km s ⁻¹)	σ_p (km s ⁻¹)	$(O - C)_s$ (km s ⁻¹)	$(O - C)_p$ (km s ⁻¹)
47480.7978	0.7569	-26.24	60.25	0.89	0.99	-0.15	-1.16
47480.9295	0.7632	-27.92	63.17	1.14	1.26	-0.59	0.48
47481.8651	0.8075	-35.51	72.50	0.91	1.01	0.78	0.54
47483.8058	0.8994	-50.13	86.33	0.98	1.08	1.08	-1.07
47513.8485	0.3220	48.76	-12.14	1.61	1.78	1.46	2.39
47514.8083	0.3675	40.24	-4.21	1.50	1.66	0.47	2.52
47518.6906	0.5513	9.00	23.99	1.39	1.54	-1.31	0.24
47526.6848	0.9298	-50.92	81.32	2.02	2.25	-2.09	-3.61
47538.7218	0.4998	15.50	16.45	1.27	1.41	-3.06	1.24
47540.7012	0.5936	3.93	29.51	0.94	1.04	0.55	-1.41
47543.6839	0.7348	-22.42	56.76	0.77	0.86	-0.66	-0.17
47544.6634	0.7812	-31.11	65.89	0.91	1.01	-0.17	-0.54
47546.7040	0.8778	-48.03	84.78	0.91	1.01	1.18	-0.55
47548.6480	0.9699	-24.31	59.46	0.87	0.96	0.25	-0.37
47550.7274	0.0683	78.92	-44.53	1.08	1.20	2.00	0.64
47554.7299	0.2579	57.28	-27.08	0.95	1.06	-1.05	-1.15
47558.6948	0.4456	25.54	8.17	1.39	1.54	-1.65	1.88
47568.6065	0.9150	-52.42	86.64	0.96	1.06	-1.36	-0.60
47569.5913	0.9616	-32.87	69.07	0.89	0.99	-0.49	1.15
47569.6698	0.9653	-27.99	63.11	0.91	1.00	1.08	-1.38
47570.6072	0.0097	28.93	7.99	0.84	0.94	0.29	3.20
47577.5864	0.3402	45.15	-13.62	0.83	0.93	0.89	-2.24
47864.8542	0.9433	-45.75	80.66	1.45	1.61	-1.54	0.50
47865.7571	0.9861	-7.69	40.86	1.87	2.07	-2.72	1.30
47866.7874	0.0348	59.01	-25.42	1.30	1.45	1.15	0.03
47868.7776	0.1291	79.34	-49.86	1.32	1.46	0.01	-2.20
47869.8006	0.1775	73.15	-41.34	1.18	1.31	0.77	-0.87
47883.7709	0.8391	-42.56	78.95	0.89	0.99	0.05	0.45
47903.7315	0.7843	-31.93	66.06	0.93	1.04	-0.36	-1.01
47904.7120	0.8307	-40.79	77.37	0.91	1.00	0.18	0.56
47905.6679	0.8760	-49.10	85.56	0.93	1.03	-0.14	0.49
47906.7301	0.9263	-49.20	84.82	1.52	1.69	0.40	-0.91
47930.6134	0.0572	71.99	-41.26	0.95	1.06	-0.82	-0.34
47934.6052	0.2462	58.54	-27.98	1.70	1.89	-1.83	0.07
47942.5941	0.6245	-0.84	36.36	0.87	0.97	0.98	0.06
48727.6172	0.7980	-33.23	70.24	0.74	0.82	1.13	0.27
49316.8629	0.7008	-16.18	50.58	1.03	1.14	-0.85	0.30
49330.7929	0.3604	40.55	-7.91	1.12	1.24	-0.37	0.02
49400.6145	0.6667	-9.17	44.14	0.89	0.99	-0.02	0.26
50003.0181	0.1925	70.08	-37.97	0.48	0.53	0.25	-0.14
50027.8831	0.3699	37.97	-6.92	0.96	1.06	-1.39	-0.61
50030.9707	0.5162	17.50	17.33	0.86	0.95	1.54	-0.57
50033.9660	0.6580	-8.13	41.78	0.82	0.91	-0.52	-0.51
50034.9653	0.7053	-16.29	51.75	0.61	0.68	-0.12	0.60
50059.8947	0.8858	-50.61	86.64	0.55	0.61	-0.44	0.32
50088.8617	0.2575	58.02	-25.57	0.50	0.55	-0.38	0.43
50092.8003	0.4440	27.65	5.77	0.88	0.98	0.20	-0.25
51239.7317	0.7550	-24.38	61.40	0.87	0.97	1.33	0.38

Appendix B: Light curve solutions for SW CMA under different limb-darkening assumptions

Tables B.1 and B.2 present our JKTEBOP solutions for fixed linear LD coefficients (u_p , u_s) from van Hamme (1993) and from Claret (2000), respectively. The uncertainties we report are formal errors from the iterative least-squares procedure, which are often found to be underestimated. In each case the agreement between the $uvby$ passbands is quite good, and the results using the different LD coefficients show small but perhaps significant systematic differences, with the inclination angle being about $0^\circ 22$ smaller using the Claret values, the sum of the radii being $\sim 0.5\%$ larger, and k also being 1–3% larger (resulting in r_p values up to 1% smaller, and r_s values 1–3% larger). Experiments using Claret coefficients for a quadratic law instead of the linear law lead to solutions that are not significantly better and results that are not very different, and tend to be closer to those obtained with the van Hamme coefficients.

Solutions with the LD coefficients free are presented in Table B.3, subject only to the condition that the coefficients be the same for the primary and secondary since their temperatures are also very similar. These results indicate slightly better agreement than before between the four passbands. On average the fitted LD coefficients are closer to those by van Hamme than those by Claret. We summarize the elements obtained from the three differ-

Table B.1. Photometric solutions for SW CMA with linear limb darkening coefficients adopted from van Hamme (1993).

Parameter	y	b	v	u
i ($^\circ$)	88.58 ± 5	88.71 ± 3	88.75 ± 3	88.53 ± 7
$e \cos \omega$	-0.30399 ± 5	-0.30314 ± 5	-0.30318 ± 5	-0.30318 ± 8
$e \sin \omega$	+0.0906 ± 13	+0.0880 ± 12	+0.0877 ± 12	+0.0900 ± 20
e	0.3163	0.3157	0.3156	0.3163
ω ($^\circ$)	163.35	163.81	163.87	163.46
$r_p + r_s$	0.1718 ± 3	0.1714 ± 3	0.1712 ± 3	0.1721 ± 4
k	0.829 ± 7	0.820 ± 4	0.819 ± 3	0.834 ± 11
r_p	0.0939	0.0942	0.0941	0.0938
r_s	0.0779	0.0772	0.0771	0.0782
u_p	0.50	0.59	0.63	0.52
u_s	0.51	0.59	0.62	0.54
y_p	0.83	0.95	1.07	1.26
y_s	0.84	0.96	1.08	1.28
J_s	1.0153 ± 13	1.0088 ± 12	0.9884 ± 12	1.0269 ± 19
L_s/L_p	0.6946	0.6777	0.6652	0.7075
σ (mmag)	5.8	5.4	5.5	8.0
N_{obs} used	818	815	820	820

Table B.2. Photometric solutions for SW CMA with linear limb darkening coefficients adopted from Claret (2000).

Parameter	y	b	v	u
i ($^\circ$)	88.34 ± 5	88.47 ± 4	88.54 ± 4	88.32 ± 7
$e \cos \omega$	-0.30295 ± 7	-0.30312 ± 5	-0.30317 ± 5	-0.30311 ± 9
$e \sin \omega$	+0.0911 ± 18	+0.0878 ± 15	+0.0870 ± 15	+0.0915 ± 26
e	0.3163	0.3156	0.3154	0.3166
ω ($^\circ$)	163.27	163.84	164.00	163.20
$r_p + r_s$	0.1729 ± 3	0.1725 ± 3	0.1721 ± 6	0.1730 ± 5
k	0.855 ± 12	0.836 ± 7	0.830 ± 6	0.864 ± 19
r_p	0.0932	0.0939	0.0940	0.0929
r_s	0.0797	0.0786	0.0781	0.0802
u_p	0.60	0.69	0.72	0.59
u_s	0.61	0.69	0.72	0.60
y_p	0.83	0.95	1.07	1.26
y_s	0.84	0.96	1.08	1.28
J_s	1.0207 ± 18	1.0142 ± 18	0.9977 ± 18	1.0255 ± 26
L_s/L_p	0.7430	0.7085	0.6871	0.7606
σ (mmag)	5.8	5.5	5.5	7.9
N_{obs} used	818	817	820	820

ent LD prescriptions in Table B.4, where the results from the separate passbands have been averaged in each case, with weights inversely proportional to the rms residual of each solution. The light elements finally adopted for the analysis of SW CMA are those with LD free, and are repeated in Table 3 of Sect. 2.3 in the main text, with more conservative errors as described there.

Appendix C: Light curve solutions for HW CMA under different limb-darkening assumptions

Table C.1 reports the results from JKTEBOP fits using linear LD coefficients from Claret (2000). The errors listed include the uncertainty in the light ratio constraint, but are otherwise internal and unrealistically small in most cases. Similarly small errors are obtained using the van Hamme (1993) coefficients. The geometric elements show good agreement between the v , b , and y bands, with u being more discrepant (and also more uncertain). Results using the LD coefficients from van Hamme (1993) are given in Table C.2, and show similarly good agreement in $uvby$. In this case we report more conservative errors from 1000 Monte Carlo simulations in which we perturbed the main adjustable quantities that were held fixed to allow their errors to propagate through: the theoretical LD coefficients were allowed to vary by ± 0.08 , $e \sin \omega$ and $e \cos \omega$ were perturbed by amounts corresponding to the spectroscopic uncertainties in e and ω , and the flux ratios J_s were al-

lowed to vary by ± 0.002 . Monte Carlo errors using LD from Claret (2000) are very similar to these.

The systematic differences between the fits with Claret and van Hamme LD coefficients are smaller than we found before for SW CMa: with the Claret coefficients the inclination angle is marginally smaller (by $0^\circ 01$), the sum of the radii is $\sim 0.5\%$ larger, and k is also 0.1% larger, all in the same direction as found for SW CMa. The individual radii are both systematically larger by about 0.5% .

The light elements we adopt for the analysis of HW CMa are those that use the van Hamme (1993) coefficients. Final values averaged over the *vby* passbands are presented in Table 7 of Sect. 3.3.

Table B.4. Weighted mean photometric solutions for SW CMa for three different treatments of the linear limb darkening coefficients.

Parameter	Free	van Hamme	Claret
i ($^\circ$)	88.59 ± 4	88.66 ± 10	88.44 ± 10
$e \cos \omega$	-0.30313 ± 9	-0.30312 ± 9	-0.30309 ± 10
$e \sin \omega$	+0.0883 ± 16	+0.0889 ± 15	+0.0889 ± 22
e	0.3157 ± 4	0.3159 ± 4	0.3159 ± 6
ω ($^\circ$)	163.76 ± 28	163.66 ± 26	163.65 ± 39
$r_p + r_s$	0.1718 ± 1	0.1715 ± 3	0.1726 ± 4
k	0.827 ± 4	0.824 ± 7	0.843 ± 15
r_p	0.0940 ± 1	0.0940 ± 2	0.0936 ± 5
r_s	0.0778 ± 2	0.0775 ± 5	0.0789 ± 9

Table B.3. Photometric solutions for SW CMa allowing the linear limb darkening coefficients to vary freely, with the condition that they be the same for the two components.

Parameter	y	b	v	u
i ($^\circ$)	88.53 ± 16	88.59 ± 12	88.62 ± 11	88.62 ± 16
$e \cos \omega$	-0.30300 ± 6	-0.30314 ± 5	-0.30318 ± 5	-0.30321 ± 7
$e \sin \omega$	+0.0902 ± 15	+0.0875 ± 14	+0.0869 ± 14	+0.0893 ± 18
e	0.3161	0.3155	0.3154	0.3161
ω ($^\circ$)	163.45	163.89	164.00	163.59
$r_p + r_s$	0.1720 ± 8	0.1719 ± 6	0.1717 ± 6	0.1716 ± 8
k	0.832 ± 18	0.826 ± 10	0.825 ± 8	0.824 ± 13
r_p	0.0939	0.0941	0.0941	0.0941
r_s	0.0781	0.0778	0.0776	0.0775
$u_p = u_s$	0.52 ± 5	0.64 ± 4	0.69 ± 4	0.50 ± 6
y_p	0.83	0.95	1.07	1.26
y_s	0.84	0.96	1.08	1.28
J_s	1.0136 ± 36	1.0121 ± 26	0.9961 ± 24	1.0188 ± 50
L_s/L_p	0.7013	0.6903	0.6771	0.6903
σ (mmag)	5.8	5.5	5.5	8.0
N_{obs} used	818	817	820	820

Table C.1. Constrained photometric solutions for HW CMa with linear limb darkening coefficients adopted from Claret (2000).

Parameter	y	b	v	u
i ($^\circ$)	84.79 ± 6	84.85 ± 7	84.85 ± 5	84.66 ± 9
$r_p + r_s$	0.06862 ± 6	0.06763 ± 8	0.06781 ± 6	0.07038 ± 10
k	1.01294 ± 4	1.01275 ± 5	1.01304 ± 4	1.01076 ± 5
r_p	0.03409	0.03360	0.03368	0.03500
r_s	0.03453	0.03403	0.03412	0.03538
u_p	0.59	0.67	0.70	0.65
u_s	0.59	0.67	0.70	0.64
y_p	0.90	1.03	1.17	1.38
y_s	0.88	1.01	1.15	1.36
J_s	1.075	1.091	1.105	1.078
L_s/L_p	1.103	1.119	1.134	1.106
σ (mmag)	4.4	5.5	4.1	7.0
N_{obs} used	415	413	409	413

Table C.2. Constrained photometric solutions for HW CMA with linear limb darkening coefficients adopted from van Hamme (1993).

Parameter	y	b	v	u
i ($^\circ$)	84.80 ± 8	84.87 ± 9	84.87 ± 8	84.67 ± 11
$r_p + r_s$	0.06829 ± 67	0.06725 ± 81	0.06741 ± 66	0.07008 ± 109
k	1.0129 ± 225	1.0107 ± 223	1.0109 ± 223	1.0108 ± 227
r_p	0.03393 ± 45	0.03345 ± 50	0.03352 ± 49	0.03485 ± 64
r_s	0.03437 ± 55	0.03380 ± 57	0.03389 ± 53	0.03523 ± 69
u_p	0.51	0.59	0.62	0.58
u_s	0.51	0.58	0.61	0.57
y_p	0.90	1.03	1.17	1.38
y_s	0.88	1.01	1.15	1.36
J_s	1.075 ± 2	1.091 ± 2	1.105 ± 2	1.078 ± 2
L_s/L_p	1.103 ± 20	1.119 ± 20	1.134 ± 21	1.106 ± 20
σ (mmag)	4.4	5.5	4.1	7.0
N_{obs} used	415	413	409	413